Extensional basin evolution in the Cordillera Blanca, Peru: Stratigraphic and isotopic records of detachment faulting and orogenic collapse in the Andean hinterland

Melissa K. Giovanni,[1] Brian K. Horton,[2] Carmala N. Garzione,[3] Brendan McNulty,[4] and Marty Grove[5]

Received 12 January 2010; revised 9 August 2010; accepted 17 August 2010; published 30 November 2010.

[1] Sedimentologic, provenance, oxygen isotope, and $^{40}Ar/^{39}Ar$ results provide insights into late Cenozoic evolution of an extensional hinterland basin in the Peruvian Andes. The 5–6.5 km Cordillera Blanca composes the glaciated footwall of a low-angle normal fault parallel to active contractional structures in the Andean fold-thrust belt. The ~200 km long, WSW dipping (19°–36°) Cordillera Blanca detachment fault accommodated >12–15 km of dip-slip displacement, inducing subsidence of the hanging-wall supradetachment basin, which is filled by ~1300 m of conglomerate, sandstone, siltstone, and limited carbonate of the upper Miocene-Pliocene Lloclla Formation. Lithofacies associations are attributed to lacustrine fan-delta to proximal, stream-dominated alluvial fan sedimentation. Provenance data record footwall unroofing of Jurassic through Miocene volcanic and sedimentary rocks during NW directed, axial dispersal of sediment. Provenance data record the appearance of footwall-derived granite clasts from the upper Miocene Cordillera Blanca batholith and a change to transverse, WSW directed transport. Variations in the character and preservation of basin fill suggest along-strike propagation of the fault through time. Initial extension and subsidence is constrained to the latest Miocene by an $^{40}Ar/^{39}Ar$ biotite age of 5.4 ± 0.1 Ma for a basal tuff in the Lloclla Formation. Estimation of paleolake water composition shows very negative $\delta^{18}O$(VSMOW) values (−13.6‰ to−18.2‰), indicating that high elevations comparable to modern were already attained in the Cordillera Blanca during earliest normal faulting and basin evolution. These results lend support to models suggesting that substantial shortening, crustal thickening, and surface uplift were necessary precursor conditions for the generation of the Cordillera Blanca detachment fault. **Citation:** Giovanni, M. K., B. K. Horton, C. N. Garzione, B. McNulty, and M. Grove (2010), Extensional basin evolution in the Cordillera Blanca, Peru: Stratigraphic and isotopic records of detachment faulting and orogenic collapse in the Andean hinterland, *Tectonics*, *29*, TC6007, doi:10.1029/2010TC002666.

1. Introduction

[2] Although extensional deformation during convergence is observed in elevated hinterlands of ancient fold-thrust belts [e.g., *Burchfiel et al.*, 1992; *Hodges and Walker*, 1992; *Axen et al.*, 1995; *Wells*, 1997], few cases of active hinterland extension have been identified in contractional retroarc systems. In the Andes of South America, small-displacement (<100 m) faults locally accommodate limited hinterland extension [*Sebrier et al.*, 1985; *Lavenu*, 1986; *Mercier et al.*, 1992], but the Cordillera Blanca of Peru is the only example of active, large-magnitude extension with pronounced footwall topography [*McNulty and Farber*, 2002]. The Cordillera Blanca (Figure 1) contains >15 peaks above 6 km and is bounded by a well-defined WSW dipping normal fault with considerable displacement and seismic activity [*Schwartz*, 1988; *Deverchere et al.*, 1989]. Possible explanations for late Cenozoic normal faulting in the Cordillera Blanca include collapse of thick crust [*Dalmayrac and Molnar*, 1981; *Sebrier et al.*, 1988a], fault reactivation [*Schwartz*, 1988], strain partitioning during convergence [*McNulty et al.*, 1998], flat-slab subduction [*McNulty and Farber*, 2002], or pluton emplacement [*Petford and Atherton*, 1992].

[3] The lack of a consensus over the mechanism(s) driving extension in the Peruvian Andes highlights the incomplete picture of the geologic history of the Cordillera Blanca and adjacent Callejon de Huaylas basin. Although the Cordillera Blanca detachment fault is active, few constraints are available on the timing of initial slip. For the corresponding supradetachment basin, uncertainty persists over controls on the timing, amount, and spatial variability of hanging-wall subsidence. Furthermore, given the Cordillera Blanca's distinction as one of the highest topographic elements of the Andes, it is important to consider the past elevation history and its relationship to earlier shortening and later extension.

[4] The goals of this study are to identify the timing and mode of extensional basin evolution along the Cordillera

[1]Department of Geoscience, University of Calgary, Calgary, Alberta, Canada.
[2]Institute for Geophysics and Department of Geological Sciences, Jackson School of Geosciences, University of Texas at Austin, Austin, Texas, USA.
[3]Department of Earth and Environmental Sciences, University of Rochester, Rochester, New York, USA.
[4]Department of Earth Sciences, California State University Dominguez Hills, Carson, California, USA.
[5]Department of Geological and Environmental Sciences, Stanford University, Stanford, California, USA.

0278-7407/10/2010TC002666

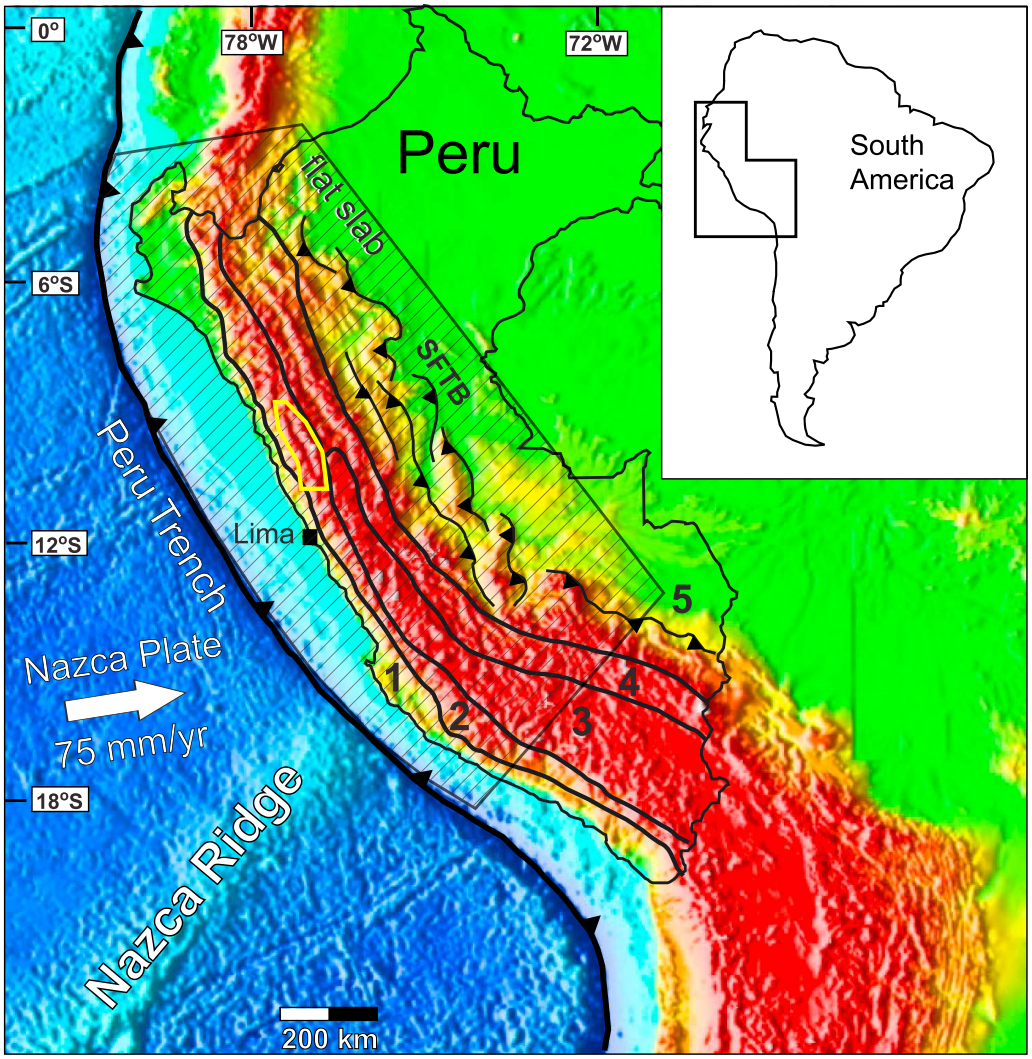

Figure 1. Simplified regional map of the Nazca-South America plate boundary showing Peruvian flat slab segment (ruled pattern) and major tectonic/physiographic zones: (1) coastal zone, (2) Western Cordillera, (3) Altiplano, (4) Eastern Cordillera, and (5) Subandean fold-thrust belt (SFTB) [after *Dalmayrac and Molnar*, 1981; *Suarez et al.*, 1983]. Small polygon shows outline of Cordillera Blanca region (Figure 2). Nazca-South America convergence rate for 12°S is from *DeMets et al*. [1994]. DEM base map from the National Geophysical Data Center, National Oceanic and Atmospheric Administration (http://www.ngdc.noaa.gov).

Blanca detachment fault in order to constrain the history of early extensional processes in the Peruvian hinterland. In addition to characterizing sediment provenance and depositional processes in the Callejon de Huaylas basin, $^{40}Ar/^{39}Ar$ geochronology of volcanic rocks and oxygen isotopic analyses of basin-fill carbonates provide insights into the absolute age of fault-induced subsidence and paleoelevation of the adjacent footwall.

2. Geologic Setting

2.1. Regional Tectonic Context

[5] Although large-magnitude extension is rare along the modern Andean margin, a zone of significant normal faulting is concentrated in the Cordillera Blanca of Peru (Figure 1). The region is situated above the modern flat-slab segment of the subducted Nazca plate [*Gutscher et al.*, 1999; *Giovanni et al.*, 2002; *Hampel*, 2002; *Rosenbaum et al.*, 2005]. The Cordillera Blanca normal fault and associated Callejon de Huaylas basin (Figure 2) are distinguished by their hinterland location and orientation perpendicular to regional E-W to ENE-WSW compression in the Andean fold-thrust belt to the east. Quaternary fault scarps and seismicity in the Cordillera Blanca provide evidence of normal faulting oriented parallel to the NNW strike of active compressional structures in the thrust belt of the Eastern Cordillera and Subandean Zone [*Yonekura et al.*, 1979; *Dalmayrac and Molnar*, 1981; *Suarez et al.*, 1983; *Schwartz*, 1988]. Micro-

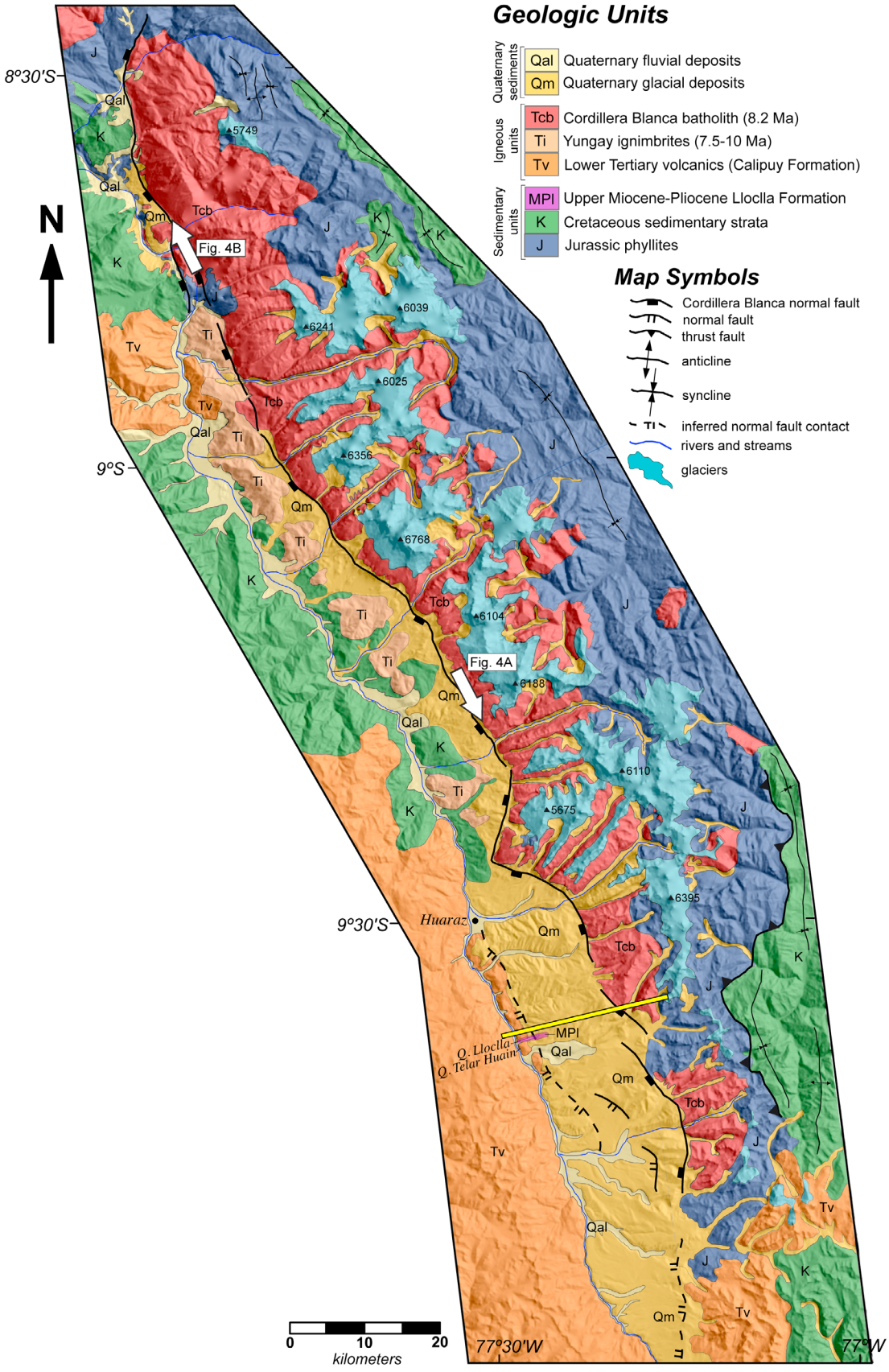
Geologic Units
Quaternary sediments
Qal Quaternary fluvial deposits
Qm Quaternary glacial deposits
Igneous units
Tcb Cordillera Blanca batholith (8.2 Ma)
Ti Yungay ignimbrites (7.5-10 Ma)
Tv Lower Tertiary volcanics (Calipuy Formation)
Sedimentary units
MPl Upper Miocene-Pliocene Llocllа Formation
K Cretaceous sedimentary strata
J Jurassic phyllites
Map Symbols
Cordillera Blanca normal fault
normal fault
thrust fault
anticline
syncline
inferred normal fault contact
rivers and streams
glaciers
N
8°30'S
9°S
9°30'S
77°30'W
77°W
Fig. 4A
Fig. 4B
Huaraz
Q. Llocllа
Q. Telar Huain
5749
6039
6241
6025
6356
6768
6104
6188
6110
5675
6395
0 10 20
kilometers

Figure 2

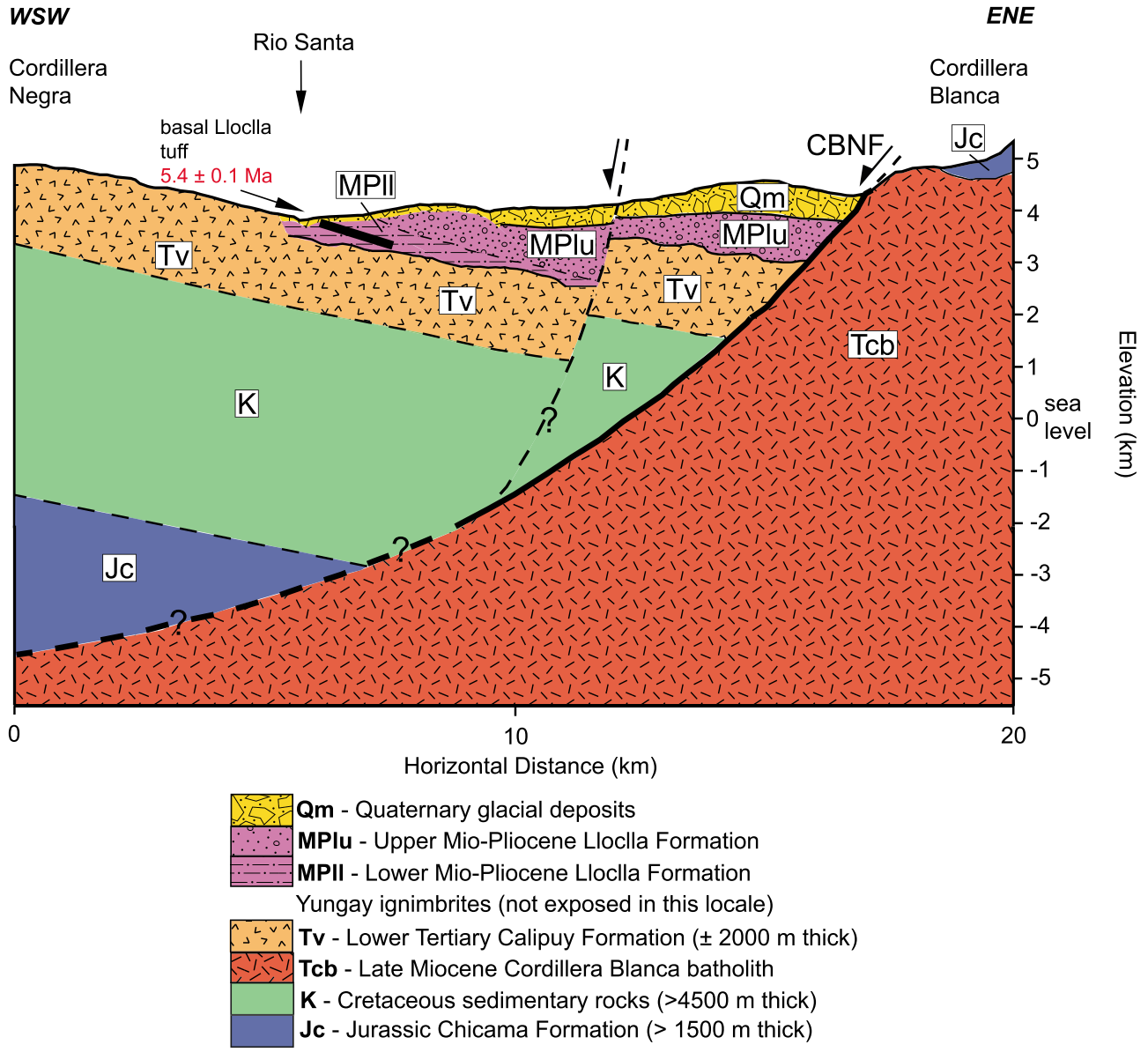

Figure 3. Schematic WSW-ENE cross section through hanging-wall supradetachment basin (location in Figure 2) adjacent to Cordillera Blanca normal fault (CBNF). Black line in lowermost Llocla Formation indicates position of basal Llocla tuff. Subsurface depiction of structural geometry is based on thicknesses reported for the Tertiary Calipuy Formation, Cretaceous sedimentary rocks and Jurassic Chicama Formation from *Cobbing et al*. [1996] and *Cobbing and Sanchez* [1996].

seismicity beneath the hanging-wall basin and earthquake focal mechanisms recorded from the 1946 Ancash earthquake (M_s = 7.2) ~100 km to the NE demonstrate the broad extent of hinterland extension [*Doser*, 1987; *Deverchere et al.*, 1989; *Bellier et al.*, 1991]. The contrast between the hinterland and frontal thrust belt has been explained by buoyancy forces arising from the gravitational body force acting on the elevated Cordillera Blanca and associated crustal root [*Dalmayrac and Molnar*, 1981; *Suarez et al.*, 1983; *Molnar and Lyon-Caen*, 1988]. This configuration results in a delicate balance between the compressive forces affecting the east flank of the Andes and the gravitational force acting on the highest parts of the orogen.

Figure 2. Geologic map of the Cordillera Blanca extensional system at ~8.5°S–10°S [from *Wilson*, 1967a, 1967b, 1967c; *Cobbing and Sanchez*, 1996]. Traces of southern fault segments are simplified from *Schwartz* [1988]. Peak elevations are listed in m. Line near Quebrada Llocla (15 km south of Huaraz) denotes the location of WSW-ENE cross section (Figure 3). Open arrows show view directions of fault photographs (Figures 4a and 4b).

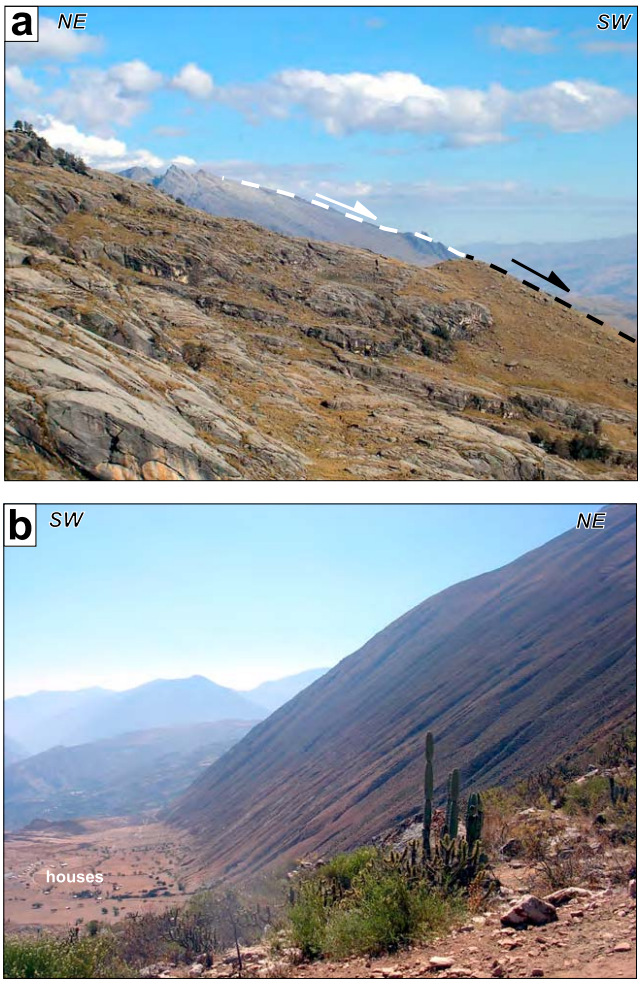

Figure 4. Photographs of the Cordillera Blanca detachment fault. (a) View SE along fault scarp. Black dashed line marks the fault in the middle ground. White dashed line marks the fault in the background. Fault dip decreases in the up-dip (NE) direction. (b) View NW along fault scarp, with houses at lower left for scale. In this region, the fault scarp is exposed for >2 km in the down-dip direction. More than 1.5 km of relief is visible in this photo.

2.2. Cordillera Blanca Extensional System

[6] At 8.5–10°S, the Cordillera Blanca defines the Pacific-Atlantic drainage divide, with peak elevations exceeding 5–6.5 km (Figure 2). The NNW trending range is bounded on its west flank by the ~200 km long Cordillera Blanca detachment fault. The WSW dipping normal fault strikes approximately N30°W (Figure 2), with dips varying from 36° in the north to 19° in the south. Directly west of the fault lies a narrow (10–15 km wide) valley occupied by an axial river, the NW flowing Rio Santa, and exposures of Miocene-Quaternary strata of the Callejon de Huaylas basin on the downthrown hanging wall (Figure 3).

[7] In the footwall, the Cordillera Blanca consists of a Neogene granodiorite (Figures 2 and 3) that intrudes the Upper Jurassic Chicama Formation and forms a steep-sided, flat-roofed batholith. The Cordillera Blanca batholith is ~200 km long by ~20 km wide and plunges to the south [*Cobbing et al.*, 1981]. The batholith is composed of Miocene granodiorite that has a reported U-Pb zircon crystallization age of 8.2 ± 0.2 Ma [*McNulty et al.*, 1998]. Adjacent to the detachment, a mylonite zone up to 1 km thick continues from the fault into the footwall batholith.

[8] Observed thicknesses for Cretaceous sedimentary units (~4.5 km) and Tertiary volcanic units (~2 km) [*Cobbing et al.*, 1996; *Cobbing and Sanchez*, 1996] constrain the subsurface geometry of the hanging wall (Figure 3). Restoration of the Jurassic-Cretaceous contact reveals 12–15 km of minimum dip-slip displacement on the detachment. This estimate is consistent with the ~3 kbar emplacement depth inferred for the Cordillera Blanca batholith on the basis of metamorphic mineral assemblages in Jurassic host rocks [*Petford and Atherton*, 1992; *McNulty and Farber*, 2002].

[9] The main strand of the Cordillera Blanca normal fault is well defined over a >120 km lateral distance with exposures exhibiting up to 2.5 km of vertical relief (Figure 4). However, ~15 km south of Huaraz, the fault breaks into several smaller segments that define a disrupted zone of step-over faults marking the structure's southern continuation (Figure 2). Fault scarps cutting Pleistocene and Holocene glacial deposits demonstrate active faulting [*Yonekura et al.*, 1979; *Schwartz*, 1988].

[10] The Callejon de Huaylas basin is a supradetachment basin [e.g., *Friedmann and Burbank*, 1995] in the hanging wall of the Cordillera Blanca detachment fault (Figures 2 and 3). Previous studies suggested accumulation coeval with Pliocene extension [*Bonnot*, 1984; *Bonnot et al.*, 1988]. Fault motion has been interpreted as principally normal slip with a left-lateral component [*Bonnot et al.*, 1988; *Sebrier et al.*, 1988b; *Petford and Atherton*, 1992; *McNulty et al.*, 1998]. Although basin fill is largely covered by younger glacial debris, the well-exposed Neogene Lloclla Formation is preserved in the southern Rio Santa valley.

2.3. Callejon de Huaylas Basin

[11] The main stratigraphic units defining the Callejon de Huaylas basin include the Miocene-Pliocene Lloclla Formation and overlying glacial deposits (Figures 2 and 3). The Lloclla Formation consists of an upward-coarsening, ~1300 m thick succession of principally conglomeratic deposits. Where exposed in the southern Rio Santa valley, it unconformably overlies the Eocene to Miocene Calipuy Formation, which yielded K-Ar biotite and muscovite ages of 52.5 ± 2.3 to 14.8 ± 2.4 Ma [*Cobbing et al.*, 1981]. Capping the Lloclla is a suite of glacial sediments, with the youngest units deposited during the last glacial maximum, estimated regionally at ~13,200 ka [*Rodbell*, 1992, 1993; *Rodbell and Seltzer*, 2000; *Farber et al.*, 2005]. Cosmogenic radionuclide (^{10}Be and ^{26}Al) ages of glacial deposits suggest regional glaciation initiated at ~1.4 Ma in Peru [*Smith et al.*, 2005].

[12] The Lloclla Formation is not preserved in the north part of the basin, where glacial deposits cap Tertiary volcanic rocks and Mesozoic sedimentary rocks (Figure 2). In the northern Rio Santa valley, up to 800 m of ignimbrites compose the upper Miocene Yungay Formation, possible

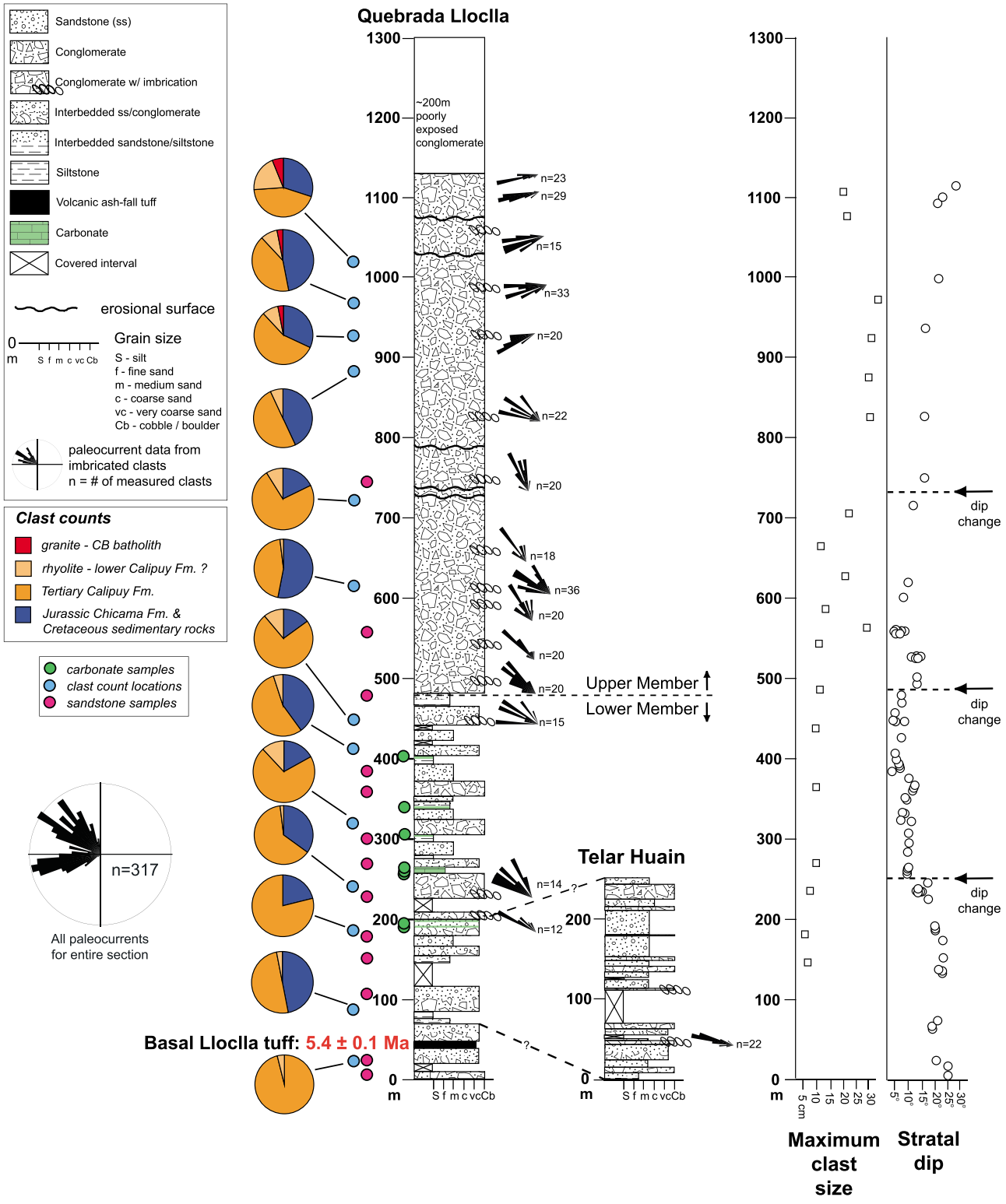

Figure 5. Measured stratigraphic section for the Lloclla Formation from Quebrada Lloclla and Telar Huain, depicting lithofacies, conglomerate clast compositions, paleocurrent orientations, carbonate and sandstone sample locations, and $^{40}Ar/^{39}Ar$ age data for the basal Lloclla tuff. Corresponding vertical plots show upsection changes in maximum clast size and stratal dip.

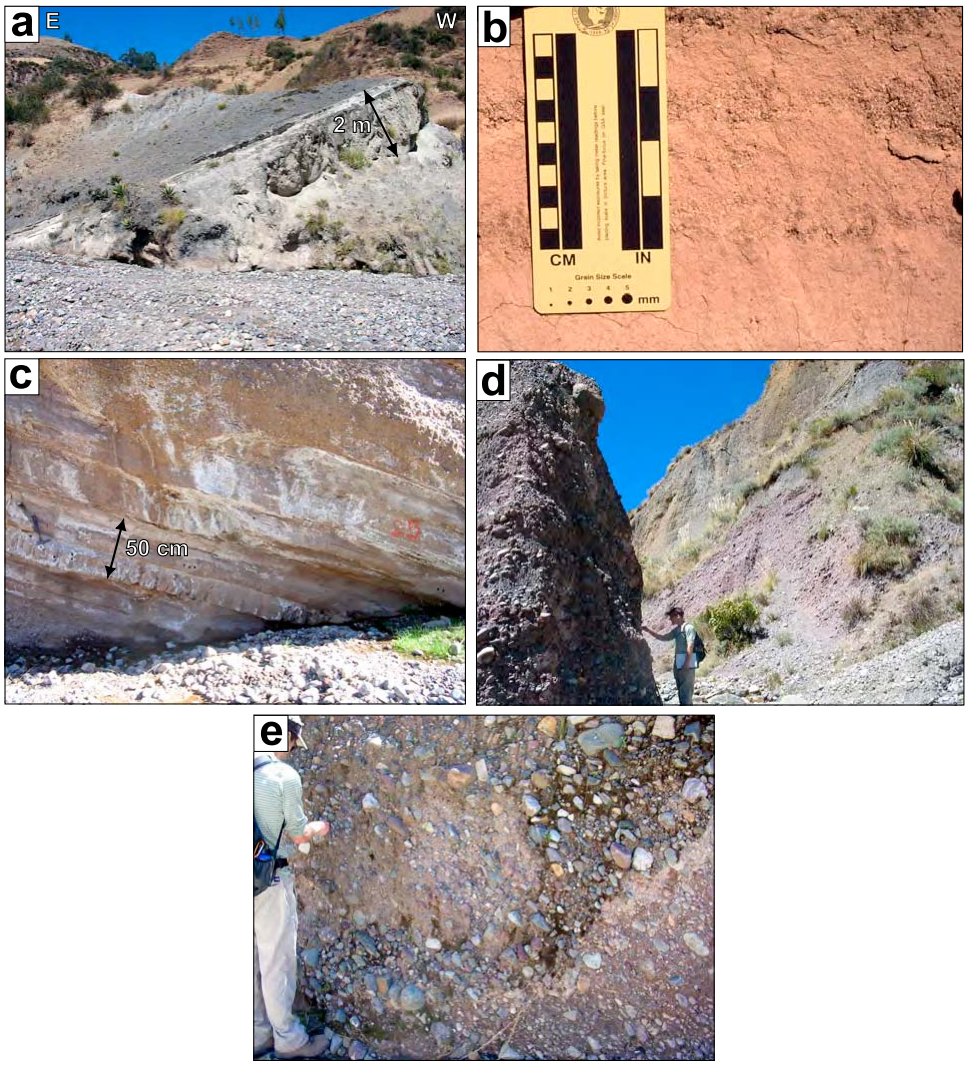

Figure 6. Photographs of representative lithofacies in the Lloclla Formation. (a) Basal Lloclla tuff (Vt). (b) Normally graded siltstone and medium-grained sandstone (Fm, Sn), Lower Member. (c) Ledge (50 cm) of freshwater carbonate (Cm) within medium-grained sandstone (Sm, Sh), Lower Member. (d) Cliffs of massive, clast-supported, cobble-boulder conglomerate (Gcm, Gci) near top of section. (e) Massive, clast-supported, cobble-boulder conglomerate with well-defined imbrication (Gci), Upper Member.

extrusive products from the Cordillera Blanca batholith. The ignimbrites unconformably overlie Jurassic and Cretaceous clastic units and Eocene to middle Miocene Calipuy volcanic rocks (Figure 2). K-Ar biotite ages from Yungay ignimbrites range from 7.6 ± 0.2 to 6.2 ± 0.2 Ma [*Cobbing et al.*, 1981]. New $^{40}Ar/^{39}Ar$ analyses of biotite grains from Yungay ignimbrites, presented below, yield ages between 8.7 ± 1.6 and 7.5 ± 0.2 Ma.

[13] A schematic cross section through the southern Rio Santa valley (near Recuay) illustrates the structural context for the Callejon de Huaylas basin, with subsurface relationships based on stratigraphic thicknesses (Figure 3). Additional constraints include angular unconformities defining basal and upper contacts of the Lloclla Formation [*Bonnot et al.*, 1988].

[14] The structural and stratigraphic configuration (Figure 3) provides insight into the unroofing pattern resulting from exhumation of the footwall of the Cordillera Blanca fault. A simple unroofing sequence would involve initial erosion of Tertiary volcanic rocks followed by Cretaceous sedimentary rocks, the Jurassic Chicama Formation, and ultimately granite of the Cordillera Blanca batholith.

3. Basin Analysis

3.1. Stratigraphy and Sedimentology

[15] The Lloclla Formation [*Bonnot*, 1984; *Bonnot et al.*, 1988] is a succession of principally clastic rocks that lies unconformably on the Eocene to middle Miocene Calipuy Formation (Figure 5) and is in angular unconformity with

Table 1. Description and Interpretation of Sedimentary Lithofacies[a]

Facies Code	Description	Interpretation	Range of Bed Thickness
Gcm	Clast-supported, massive cobble-boulder conglomerate. Poorly sorted, subrounded to rounded clasts, weak normal grading, no imbrication, occasional erosional scours.	High-energy stream flow	>2 m[b]
Gcmi	Clast-supported, massive cobble-boulder conglomerate with imbrication. Poorly sorted, subrounded to rounded clasts.	Traction bedload transport; longitudinal bars	>2 m[b]
Gchi	Clast-supported, pebble conglomerate with imbrication, medium-to well-sorted, horizontal stratification.	Longitudinal bedforms, lag deposits	>2 m[b]
Gcl	Clast-supported, pebble conglomerate with low-angle stratification, scoured basal contacts, interbedded coarse-grained sandstone lenses.	Transverse bar, channel fill	<50 cm
Sm	Massive sandstone. Medium-to coarse-grained, moderately sorted.	Rapid deposition, hyperconcentrated flow	<50 cm
Sh	Horizontally laminated sandstone. Medium-to coarse-grained, some contorted bedding. Moderately to well sorted.	Sheetflow, upper flow regime conditions	10–30 cm
Sn	Normally graded sandstone. Medium-to coarse-grained.	Channel fill, deposition by waning currents, or turbidity currents	10–30 cm
Fm	Massive siltstone. Thinly bedded.	Suspension fallout	1–10 cm
Fl	Horizontally laminated siltstone.	Suspension fallout	1–10 cm
Cm	Massive carbonate. Thinly bedded, gastropod fossils	Carbonate precipitation in shallow lake	10–30 cm
Vt	Volcanic tuff. Quartz, euhedral biotite and sanidine, well-sorted, horizontal laminations.	Pyroclastic ash-fall deposition and subaqueous suspension settling	7 m

[a]After *Miall* [1985, 1996], *Ridgway and DeCelles* [1993], *Horton and Schmitt* [1996], and *Uba et al*. [2005].
[b]Conglomerate beds are commonly amalgamated making bed contacts difficult to identify.

subhorizontal Quaternary glacial deposits tens to hundreds of m thick. The Lloclla Formation, divided into a Lower Member and Upper Member, is exposed ~15 km south of Huaraz (Figure 2) in Quebrada Lloclla and Quebrada Telar Huain with a total preserved thickness of ~1300 m (Figure 5). Exposures exist only in deeply incised ravines, making lateral bed-to-bed correlation difficult, particularly within coarse-grained intervals. The basal Lloclla tuff is best exposed in Quebrada Lloclla (Figure 6a).

[16] Two stratigraphic sections measured in the Lloclla Formation provide the basis for the definition of sedimentary lithofacies and interpretations of depositional processes (Figure 5 and Table 1). Eleven lithofacies are grouped into four facies associations interpreted to record depositional processes in different environments (Table 2).

3.1.1. Facies Association 1: Basal Volcanic Tuff

3.1.1.1. Description

[17] This facies association is limited to the Lower Member and is distinguished by a ~7 m thick, dark gray tuff that dips ~25°E toward the Cordillera Blanca normal fault (Figures 3 and 6a). The basal Lloclla tuff is identified as a separate volcanic lithofacies (Vt) because it is a distinct unit

Table 2. Facies Associations and Related Lithofacies

Facies Association	Lithofacies	Total Stratigraphic Thickness	Interpretation and Depositional Environment	Occurrence Within Lloclla Formation
1. Basal volcanic tuff	Vt	7 m	Ash-fall, lacustrine	Lower Member
2. Thin massive carbonate and interbedded fine-grained sandstone and siltstone	Cm, Sh, Sn, Fm, Fl	<4 m (carbonate), ~200 m (sandstone/siltstone)	Lacustrine, distal-fan delta	Lower Member
3. Thin pebble conglomerate and medium-grained sandstone	Gcl, Sh, Sn	~300 m	Fluvial channel in periods of high precipitation (middistal stream-dominated alluvial fan)	Lower Member
4. Coarse-grained sandstone and thick cobble-boulder conglomerate	Sm, Sh, Gcm, Gcmi, Gchi	<2 m (sandstone) >600 m (conglomerate)	Sandy braided channel (midstream-dominated alluvial fan); Gravelly braided channel (proximal stream-dominated alluvial fan)	Upper Member

restricted to the base of the section. It is comprised of well-sorted ash material with common horizontal laminations and crystals of quartz and euhedral biotite and sanidine (Table 1).

3.1.1.2. Interpretation

[18] Facies association 1 is interpreted as the result of volcanic ash accumulation in a low-energy subaqueous environment. Although preservation of primary volcanic ash is indicative of little to no reworking, horizontal laminations are suggestive of suspension settling in an offshore lacustrine environment [*Horton and Schmitt*, 1996; *Garzione et al.*, 2003]. Interpretation of a lacustrine setting is preferred over a fluvial overbank/floodplain environment due to the lack of channelized facies and presence of interbedded fine-grained sandstone and siltstone of facies association 2 above and below the tuff.

3.1.2. Facies Association 2: Thin Massive Carbonate Interbedded With Fine-Grained Sandstone and Siltstone

3.1.2.1. Description

[19] Facies association 2 is dominated by gastropod-bearing freshwater carbonate (Cm) occurring in 10–30 cm thick beds (Figures 5 and 6c). The beds are subplanar, blocky, and massive. Interbedded with the carbonates are mostly subplanar beds of well-sorted, fine-grained sandstone (Sh) with occasional normal grading (Sn), and massive to laminated siltstone (Fm, Fl) (Figure 6b). Individual clastic beds are relatively thin (several centimeters), persist laterally for tens of meters, and exhibit nonerosional bases defining broadly tabular bedding geometries. Although rare, a few clast-supported conglomerates are present in 10–30 cm thick beds (see facies association 3).

3.1.2.2. Interpretation

[20] Deposition of facies association 2 is interpreted to have occurred in a transitional zone between a nearshore lacustrine environment and the subaerially exposed outer "fan-fringe" of a fan-delta [e.g., *Nemec and Steel*, 1988; *Ridgway and DeCelles*, 1993; *Horton and Schmitt*, 1996]. Characteristics of both subaqueous and subaerial environments are observed in this facies association. Interbedded carbonate, sandstone, and conglomerate suggest that episodic clastic deposition alternated with quiet water conditions that permitted carbonate precipitation from lake waters. It is likely that the carbonate-bearing intervals, at the 200–400 m level in the measured section (Figure 5), were deposited in a shallow water lacustrine environment. Normal grading of sandstone is suggestive of deposition by turbidity currents. Massive to very weakly laminated siltstones were deposited by suspension fallout. Observed facies changes and rapid coarsening above the 400 m level suggest that subaerial fan-delta processes, particularly sheetflow processes, were responsible for transport of coarser sediments to more distal part of the fan-delta [*Leeder*, 1999].

3.1.3. Facies Association 3: Thin Pebble Conglomerate and Medium-Grained Sandstone

3.1.3.1. Description

[21] This facies association occurs throughout the Lower Member. Sandy pebble conglomerate with low-angle stratification (Gcl), sandstone lenses, and basal scours alternate with moderately sorted, medium-to coarse-grained sandstone with occasional normal grading (Sn) and horizontal lamination (Sh). Sandstone beds are 10–30 cm thick and the thickest conglomerate beds are ~50 cm thick. Conglomerate beds are commonly amalgamated, with bed contacts becoming harder to distinguish upsection.

3.1.3.2. Interpretation

[22] Facies association 3 is interpreted to have been deposited in the intermediate zone of a stream-dominated alluvial fan, with most deposition taking place in sandy and gravelly bars within fluvial channels that reach the subaerial "fan-fringe" where it transitions to a fan-delta [e.g., *Miall*, 1985, 1996; *Ridgway and DeCelles*, 1993; *Leeder*, 1999]. In places, particularly in the uppermost Lower Member, conglomeratic sandstones with non-erosive bed contacts are interpreted as the products of sheetfloods in more distal fan environments [e.g., *Blair and McPherson*, 1994; *Hampton and Horton*, 2007]. Observed coarsening trends within conglomeratic packages may be the result of lateral migration of channels across the surface of the alluvial fan [*Miall*, 1977; *Uba et al.*, 2005].

3.1.4. Facies Association 4: Coarse-Grained Sandstone and Thick Cobble-Boulder Conglomerate

3.1.4.1. Description

[23] Facies association 4 includes the majority of the Upper Member, beginning at the ~600 m level (Figures 5, 6d, and 6e). The Upper Member is defined by very thick beds of clast-supported conglomerate that are predominantly imbricated (Gcmi) with a few erosional surfaces. These deposits are interbedded with thin beds of lenticular coarse-grained sandstone. An upward-coarsening sequence is observed within the cobble-boulder conglomerate. Mean clast size ranges from 6 cm at the 500 m level to 14 cm at the top of the section. Lithofacies include (1) clast-supported pebble-boulder conglomerates with imbrication (Gcmi), (2) massive, nonimbricated, poorly sorted conglomerates with occasional erosional scours (Gcm), (3) sandy, well-sorted, pebble conglomerate with horizontal stratification (Gchi), and (4) occasional lenses of coarse-grained sandstone (Sm, Sh). The uppermost levels of the Upper Member are covered in angular unconformity by Quaternary glacial deposits.

3.1.4.2. Interpretation

[24] Deposition of facies association 4 is attributed to gravel bars in poorly defined low-sinuosity channels and sediment gravity flows in the proximal sector of a stream-dominated alluvial fan [e.g., *Miall*, 1985; *Ridgway and DeCelles*, 1993; *Miall*, 1996; *Leeder*, 1999]. The upsection increase in mean clast size (Figure 5) suggests progradation of the fan system toward distal regions. The uppermost basin fill may have been deposited at the fan apex, where channelized and nonchannelized facies are closely associated. Large-scale upward-coarsening sequences are observed in prograding fans where depositional processes are increasingly proximal. Progradation may be caused by increasing intensity of basin-margin faulting or an increasingly humid climate causing higher runoff and sediment transport rates [*Leeder*, 1999].

3.2. Stratigraphic Variations in Stratal Dip

[25] E-dipping strata of the Lloclla Formation cap the E-tilted hanging wall of the Cordillera Blanca normal fault. Stratal dip variations within the Lloclla Formation reveal four

Table 3. Parameters for Sandstone Point Counts

Symbol	Grain Categories	Recalculated Parameters
Qm	Monocrystalline quartz	*Q-F-L*
Qp	Polycrystalline quartz	Q = Qm + Qp
P	Plagioclase feldspar (includes Na and Ca varieties)	F = P + K
K	Potassium feldspar	L = Lv + Ls + Lm
Lvm	Microlitic volcanic grains	
Lvl	Lathwork volcanic grains	*Lm-Lv-Ls*
Lvf	Felsic volcanic grains	Lm
Lm	Metamorphic lithic grains (phyllite)	Lv = Lvm + Lvl + Lvf
Lsh	Mudstone	Ls = Lsh + Lc
Lc	Carbonate	
		Qm-P-K
		Qm
		P
		K

groups (Figure 5). In the Lower Member, dips range between 25°NE and 15°NE from the 0 to 250 m level (Figure 5). At 250 m, dips shallow abruptly to 10° and range from 5° to 10° up to 475 m, which marks the base of the Upper Member (Figure 5). From 475 to 725 m, dips range from ~7° to 15°. Above 725 m, bedding is not well defined in the thick, massive conglomerate of the Upper Member, but dips apparently steepen from ~15° to 30° (Figure 5).

[26] Upsection variations in stratal dip are considered the product of progressive syndepositional tilting during basin evolution. The principal trend toward shallower dips upsection is suggestive of a broad growth stratal package related to east-down tilting of the hanging wall during deposition. Such basin infill patterns are commonly attributed to motion on a listric normal fault. However, an upsection steepening of dips suggests further complexity that may be related to variations in the geometry of master or subsidiary faults [*Gibbs*, 1984].

3.3. Conglomerate and Sandstone Provenance

[27] The provenance of clastic sediment in the Lloclla Formation was determined using sandstone compositional data collected from petrographic analysis (point counts), conglomerate compositional data from clast counts, and sediment dispersal patterns from paleocurrent measurements. Most compositional data were collected from the measured section at Quebrada Lloclla (Figure 5).

[28] Petrographic thin sections were cut from primarily medium-grained sandstone and stained for plagioclase and potassium feldspar. Thirteen samples were counted using a modified Gazzi-Dickinson method [*Ingersoll et al.*, 1984]. Petrographic parameters (Table 3) and recalculated detrital modes (Table 4) are based on methods described by *Ingersoll et al.* [1984] and *Dickinson* [1985]. Recalculated detrital modes are plotted on ternary diagrams (Figure 7) depicting ratios of quartz-feldspar-lithic fragments (Q-F-L), monocrystalline quartz-plagioclase-K-feldspar (Qm-P-K) and metamorphic-volcanic-sedimentary lithic fragments (Lm-Lv-Ls). The compositional data are divided into four groups on the basis of stratigraphic m level, where the most striking feature is the predominance of lithic grains, as shown by the Q-F-L diagram (Figure 7). The feldspar grains are dominantly plagioclase feldspar, a trend visible in the Qm-P-K diagram (Figure 7). The Lm-Lv-Ls diagram reveals a moderate upsection trend of increasing volcanic lithic grains (Figure 7). The mean sandstone compositions, reported as percentages, are Q-F-L (13-13-74), Qm-P-K (51-44-5), and Lm-Lv-Ls (28-66-6).

[29] Conglomerates are predominantly clast supported, with some imbrication, and subrounded to rounded pebbles and boulders (Figures 6d and 6e). Clast counts were conducted every 40–50 m of stratigraphic section (Figure 5). Each of 13 clast counts identified lithologies of 100–125 individual clasts within 1 m^2 of a single bed. Clast types were grouped into metapelites of the Jurassic Chicama Formation, volcanic rocks of the Tertiary Calipuy Formation, rhyolite probably from the Tertiary Calipuy Formation (rather than the poorly consolidated Tertiary Yungay ignimbrites), and granite from the Cordillera Blanca batholith. The lower 900 m of the measured section are dominated by clasts of the Tertiary Calipuy Formation, with granite clasts first appearing above 900 m (Figure 8).

[30] Paleocurrent data were collected every ~50 m of section as lithofacies allowed. Where clast imbrication was observed, an average of 20 clast orientations was measured. Rose diagrams for each site are plotted according to stratigraphic level (Figure 5). In addition, a total of 317 clast measurements are plotted in a cumulative rose diagram that reveals two paleoflow directions (Figure 8). The lower 900 m exhibit a mean paleoflow direction to the NW (314°). Above 900 m, flow direction changes to a more WSW orientation (260°) (Figures 5 and 8).

3.4. Age Constraints

[31] $^{40}Ar/^{39}Ar$ age results for the Yungay Formation and basal tuff of the Lloclla Formation help define the onset of

Table 4. Recalculated Modal Point-Count Data for Sandstones

Sample Q. Lloclla:	Level (m) 9°38.5′S, 77°29.3′W	Sampling Elevation (m)	Q-F-L %			Qm-P-K %			Lm-Lv-Ls %		
			Q	F	L	Qm	P	K	Lm	Lv	Ls
LL5	5	3369	53	56	321	43	53	3	164	152	5
LL23	23	3387	22	28	133	17	28	0	55	76	2
LL102	102	3466	59	119	260	57	104	15	76	148	36
LL144	144	3508	28	35	199	28	35	0	45	135	19
LL237	237	3601	26	10	198	25	10	0	52	131	15
LL261	261	3625	55	61	208	55	47	14	30	170	8
LL561	561	3925	42	30	377	40	30	0	55	299	23
LL739	739	4103	30	5	198	29	5	0	39	148	11

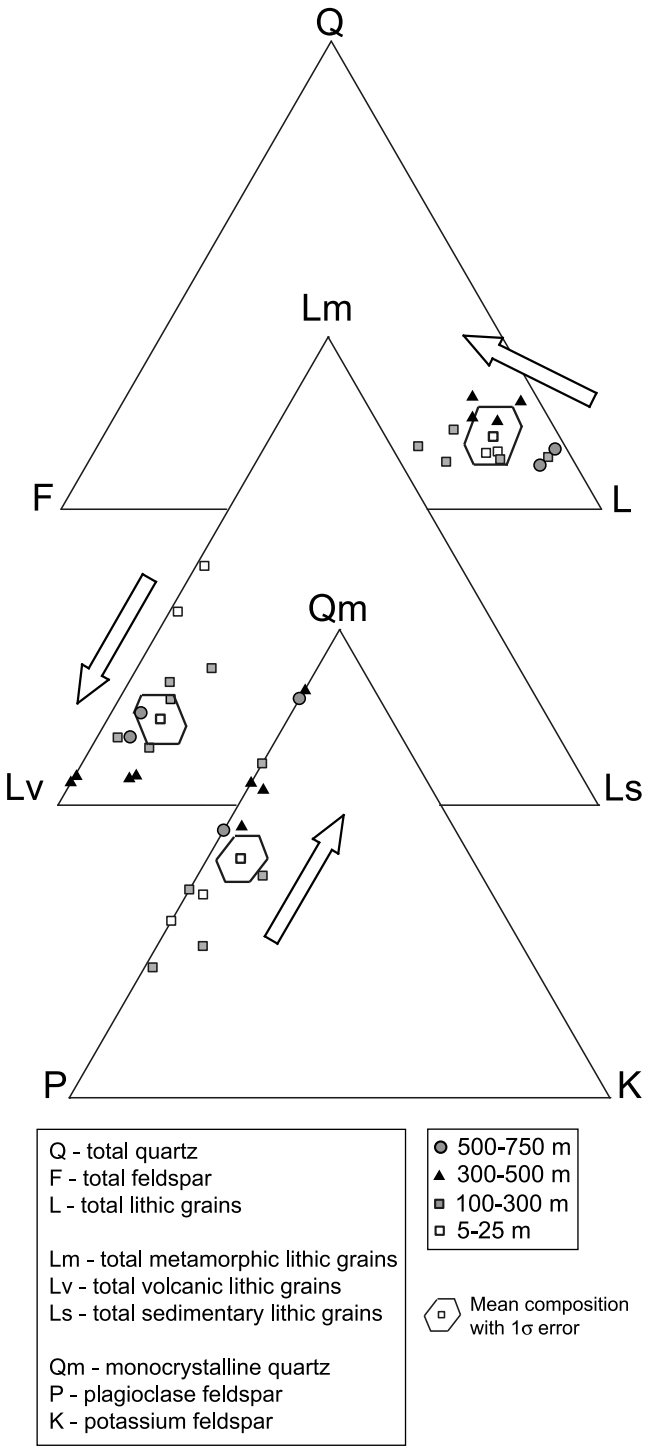

Figure 7. Compositional ternary diagrams (Q-F-L, Lm-Lv-Ls, and Qm-P-K) for 13 sandstone samples of the Llocla Formation (see Table 2). Four symbols correspond to sampled stratigraphic level (Figure 5). Arrows indicate upsection trends in detrital compositions.

hanging-wall subsidence along the Cordillera Blanca detachment fault. Biotite grains from the Yungay ignimbrites and basal Llocla tuff were separated using magnetic separation techniques, handpicked for purity, and then packed into Cu foil packets. Five to eight milligrams of biotite grains from each sample were irradiated with sanidine flux monitors (Fish Canyon Tuff: nominal age of 27.8 ± 0.5 Ma) [*Renne et al.*, 1994] at the Ford reactor, University of Michigan for 45 h. Step-heating analyses were carried out at the University of California, Los Angeles in a double-vacuum resistance furnace with a Ta crucible. Isotopic ratios were measured using a VG1200 gas source automated mass spectrometer. An in-house data reduction program was used to reduce the raw data and calculate ages. Reported ages represent weighted mean ages with errors reported at the 1σ level. Weighted mean ages do not include uncertainties in the J factor or decay constants, as appropriate for samples analyzed in a single lab with the same flux monitors [*McDougall and Harrison*, 1999].

[32] Three samples from the Yungay Formation provide constraints on ignimbrite deposits in the northern Rio Santa valley. $^{40}Ar/^{39}Ar$ analyses of biotite grains from Yungay ignimbrites yield variable results (Figure 9 and Table 5). One sample produced a relatively well-defined age spectrum that indicates an age of 7.5 ± 0.2 Ma (Figure 9a). The other two samples are characterized by somewhat irregular

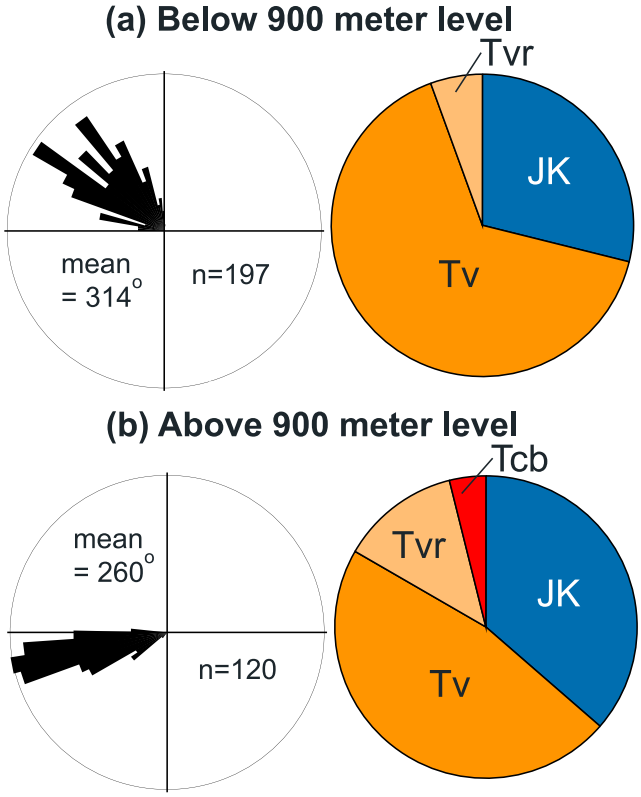

Figure 8. Paleocurrent and clast composition data for the Llocla Formation (a) below 900 m level and (b) above 900 m level. Paleocurrents show an abrupt change from NW directed to WSW directed transport above the 900 m stratigraphic level. Clast compositions record proportions of Jurassic-Cretaceous sedimentary rocks (JK), Tertiary Calipuy volcaniclastic rocks (Tv), probable lower Calipuy rhyolites (Tvr), and the appearance of Cordillera Blanca granite (Tcb) above the 900 m level.

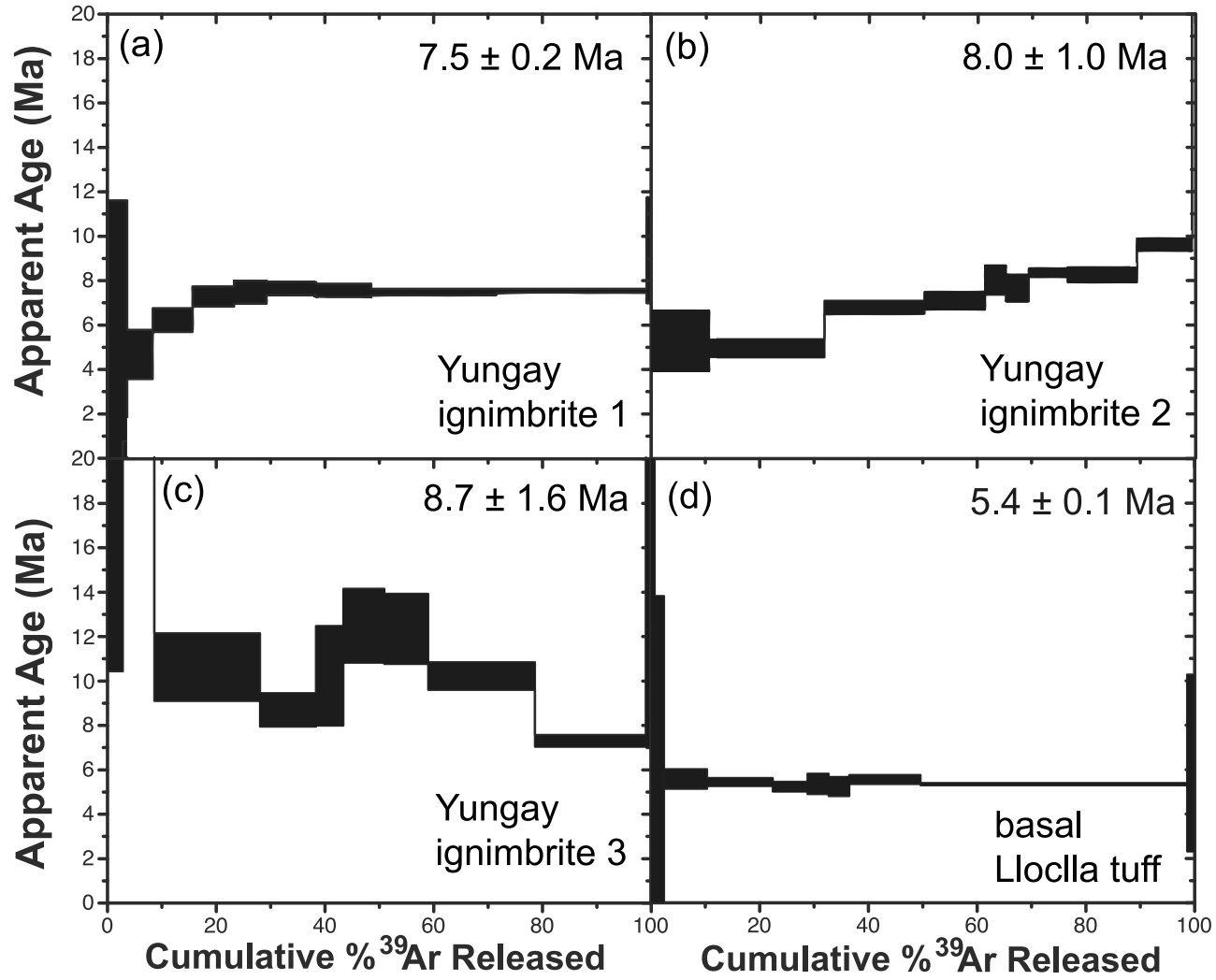

Figure 9. $^{40}Ar/^{39}Ar$ age spectra for biotite grains from (a–c) Yungay ignimbrites and (d) basal Lloclla tuff of the Callejon de Huaylas basin. Reported ages represent weighted mean ages with 1σ standard errors.

age spectra (Figures 9b and 9c) that could reflect modest amounts of excess argon [*McDougall and Harrison*, 1999]. Although all three samples yield weighted mean ages that are indistinguishable, the latter samples yield relatively large errors (8.0 ± 1.0 and 8.7 ± 1.6 Ma). For this reason, the age of ignimbrite deposition is considered to have a clear record at 7.5 Ma, with a possibility of slightly older ignimbrite volcanism that could be as old as 8–10 Ma. These results are broadly consistent with K-Ar biotite ages of 6.2 ± 0.2 to 7.6 ± 0.2 Ma reported for the Yungay ignimbrites [*Cobbing et al.*, 1981].

[33] In the Callejon de Huaylas basin, the base of the Lloclla Formation (Quebrada Lloclla section; Figure 5) contains a ~7–8 m thick, dark gray tuff that dips ~25°E toward the Cordillera Blanca normal fault (Figure 6a). *Bonnot* [1984] reported a biotite K-Ar age of 5.4 Ma (no errors reported) for the basal Lloclla tuff in Quebrada Lloclla. New $^{40}Ar/^{39}Ar$ analyses of biotite yield a weighted mean age of 5.4 ± 0.1 Ma based on a well-defined plateau age spectrum (Figure 9d), confirming the age of *Bonnot* [1984]. Importantly, this $^{40}Ar/^{39}Ar$ age for the base of the upward-coarsening Lloclla Formation indicates that basin subsidence, hence detachment faulting, commenced in this region at ~5.4 Ma.

4. Stable Isotope Methods and Results

4.1. Methods

[34] Lacustrine carbonates are porous, poorly indurated, massive to laminated, very calcareous, with moderate amounts of clay and organic matter. We examined each sample under a stereoscopic microscope to identify representative material for sampling and to identify potential diagenetic phases. All samples are micritic and show no evidence of dissolution, sparry recrystallization, or cementation. Their high primary porosity is consistent with the observation that they lack secondary diagenetic calcite. Samples were crushed to a fine powder using a mortar and pestle. Powdered samples were reacted with 30% H_2O_2 for 20 min to remove organic material prior to analysis.

Table 5. $^{40}Ar/^{39}Ar$ Step-Heating Analytical Results

T (°C)	$^{40}Ar/^{39}Ar$	$^{38}Ar/^{39}Ar$	$^{37}Ar/^{39}Ar$ ($\times 10^{-3}$)	$^{36}Ar/^{39}Ar$ ($\times 10^{-3}$)	^{39}Ar (mol) ($\times 10^{-15}$)	$\Sigma^{39}Ar$	% $^{40}Ar^*$	$^{40}Ar^*/^{39}Ar_K$	$\pm\sigma_{40/39}$	Age (Ma)	$\pm\sigma_{Age}$
Basal Lloclla Tuff: Biotite (6.1 mg; J = 0.003587). 9°38.5′S, 77°29.3′W											
500	71.604	0.1466	52.735	232.96	4.960	1.01	3.81	2.73	1.10	17.79	7.15
700	28.871	0.0870	9.492	92.146	38.337	8.79	5.57	1.60	0.29	10.49	1.95
770	3.297	0.0691	4.717	8.012	58.369	20.65	27.12	0.89	0.04	5.84	0.31
840	1.541	0.0673	3.223	2.275	70.038	34.88	54.07	0.83	0.02	5.45	0.17
900	2.273	0.0670	5.172	4.626	20.967	39.13	38.23	0.87	0.07	5.70	0.48
960	3.587	0.0686	8.746	8.890	11.383	41.45	25.72	0.92	0.14	6.05	0.96
1020	3.781	0.0667	10.797	9.768	9.050	43.28	22.64	0.86	0.17	5.62	1.14
1080	3.692	0.0683	8.413	9.148	19.975	47.34	25.79	0.95	0.10	6.23	0.65
1150	2.193	0.0664	4.439	4.286	61.452	59.82	40.64	0.89	0.03	5.83	0.21
1350	1.558	0.0655	12.274	2.104	197.790	99.99	57.92	0.90	0.01	5.90	0.08
Total gas age: 5.46 ± 0.91 Ma											
Weighted mean age: 5.40 ± 0.05 Ma											
Yungay Ignimbrite 1: Biotite (6.1 mg; J = 0.003525). 8°57.5′S, 77°48.8′W											
500	61.391	0.1118	69.275	204.766	16.321	3.64	1.39	0.86	0.98	5.43	6.19
600	15.031	0.0816	248.674	48.336	20.929	8.31	4.89	0.74	0.17	4.68	1.11
700	7.164	0.0737	83.883	20.840	33.088	15.69	13.65	0.98	0.08	6.22	0.53
770	3.800	0.0671	29.028	8.875	33.991	23.28	30.04	1.15	0.07	7.28	0.45
840	3.634	0.0669	28.170	8.212	26.715	29.24	32.18	1.18	0.08	7.47	0.52
900	3.380	0.0686	19.942	7.258	40.904	38.37	35.47	1.20	0.05	7.64	0.31
960	3.424	0.0691	20.274	7.450	45.529	48.52	34.65	1.19	0.05	7.56	0.30
1050	2.452	0.0650	14.448	4.203	103.395	71.59	47.95	1.18	0.02	7.48	0.15
1150	1.740	0.0656	29.478	1.767	123.414	99.13	68.05	1.19	0.02	7.54	0.10
1350	8.037	0.0680	152.832	22.119	3.834	99.99	18.05	1.48	0.37	9.40	2.35
Total gas age: 7.23 ± 0.61 Ma											
Weighted mean age: 7.49 ± 0.09 Ma											
Yungay Ignimbrite 2: Biotite (6.0 mg; J = 0.003525). 8°58.7′S, 77°48.3′W											
500	37.243	0.1099	20.612	123.110	46.602	10.53	2.24	0.83	0.21	5.29	1.35
600	7.827	0.0698	20.893	23.743	93.847	31.73	9.95	0.78	0.06	4.95	0.40
700	5.982	0.0687	16.905	16.515	81.517	50.15	17.88	1.07	0.05	6.80	0.30
770	5.511	0.0681	15.466	14.759	49.279	61.28	20.25	1.12	0.06	7.10	0.39
840	5.136	0.0668	13.827	12.996	16.814	65.08	24.45	1.26	0.10	8.02	0.66
900	5.164	0.0687	17.258	13.282	18.661	69.30	23.24	1.21	0.10	7.66	0.60
960	5.204	0.0702	17.306	13.051	31.565	76.43	25.21	1.32	0.03	8.35	0.19
1050	5.150	0.0690	16.778	12.919	56.564	89.21	25.21	1.30	0.05	8.25	0.33
1150	3.731	0.0658	58.573	7.399	44.701	99.31	40.51	1.52	0.04	9.62	0.28
1350	15.390	0.0403	56.576	14.251	3.076	99.99	71.61	11.15	0.42	69.56	2.56
Total gas age: 7.39 ± 0.48 Ma											
Weighted mean age: 8.02 ± 0.99 Ma											
Yungay Ignimbrite 3: Biotite (6.0 mg; J = 0.003525). 8°59.8′S, 77°48.3′W											
500	154.813	0.1558	166.610	513.688	6.703	2.81	1.94	3.00	1.36	18.98	8.55
600	70.165	0.1091	117.649	225.455	13.872	8.62	5.01	3.52	0.23	22.25	1.45
700	30.565	0.0869	76.402	97.676	46.380	28.05	5.48	1.68	0.24	10.62	1.53
770	14.914	0.0729	53.668	45.733	24.587	38.35	9.18	1.37	0.12	8.70	0.75
840	31.105	0.0801	84.061	99.716	12.043	43.39	5.18	1.61	0.35	10.23	2.24
900	34.693	0.0919	85.951	110.652	18.040	50.95	5.67	1.97	0.26	12.48	1.67
960	21.457	0.0826	72.663	65.931	19.171	58.98	9.06	1.95	0.25	12.34	1.58
1050	11.241	0.0751	60.406	32.492	46.913	78.63	14.33	1.61	0.10	10.22	0.62
1150	3.011	0.0691	73.044	6.202	48.715	99.04	38.09	1.15	0.04	7.31	0.27
1350	14.617	0.0158	26.338	13.110	2.297	99.99	72.07	10.71	0.54	66.87	3.34
Total gas age: 11.39 ± 1.28 Ma											
Weighted mean age: 8.69 ± 1.54 Ma											

[35] Water $\delta^{18}O$ and D/H and carbonate $\delta^{18}O$ and $\delta^{13}C$ were measured on a Thermo Electron Corporation Delta plus XP mass spectrometer in continuous flow mode at the University of Rochester. Water $\delta^{18}O$ was measured using an automated Gasbench II CO_2-H_2O equilibration unit. The isotope ratio was calculated using internal lab standards calibrated using VSMOW (Vienna Standard Mean Ocean Water) and VSLAP (Vienna Standard Light Antarctic Precipitation). Precision is better than ±0.08‰ for the $\delta^{18}O$ values of water. D/H was measured using a Thermo Electron TC/EA peripheral and a GC-PAL autosampler. Approximately 200 nL of sample water was injected into the TC/EA during three successive injections. The reactor was set at a temperature of 1450°C and the GC oven was set at 90°C. The average of three injections indicates a 1σ error of ±1.5‰ for δD. We report the average of six ratios (two separate runs), that yielded 1σ errors of ±1.4‰. $\delta^{18}O$ and $\delta^{13}C$ of carbonates were measured using the Gasbench II

peripheral device. Powdered samples were reacted with phosphoric acid to liberate CO_2. The isotope ratio was calculated using repeated measurements of three in-house standards calibrated using NBS-19 and NBS-18. The 1σ errors were ±0.1‰ for $\delta^{18}O$ and ±0.05‰ for $\delta^{13}C$.

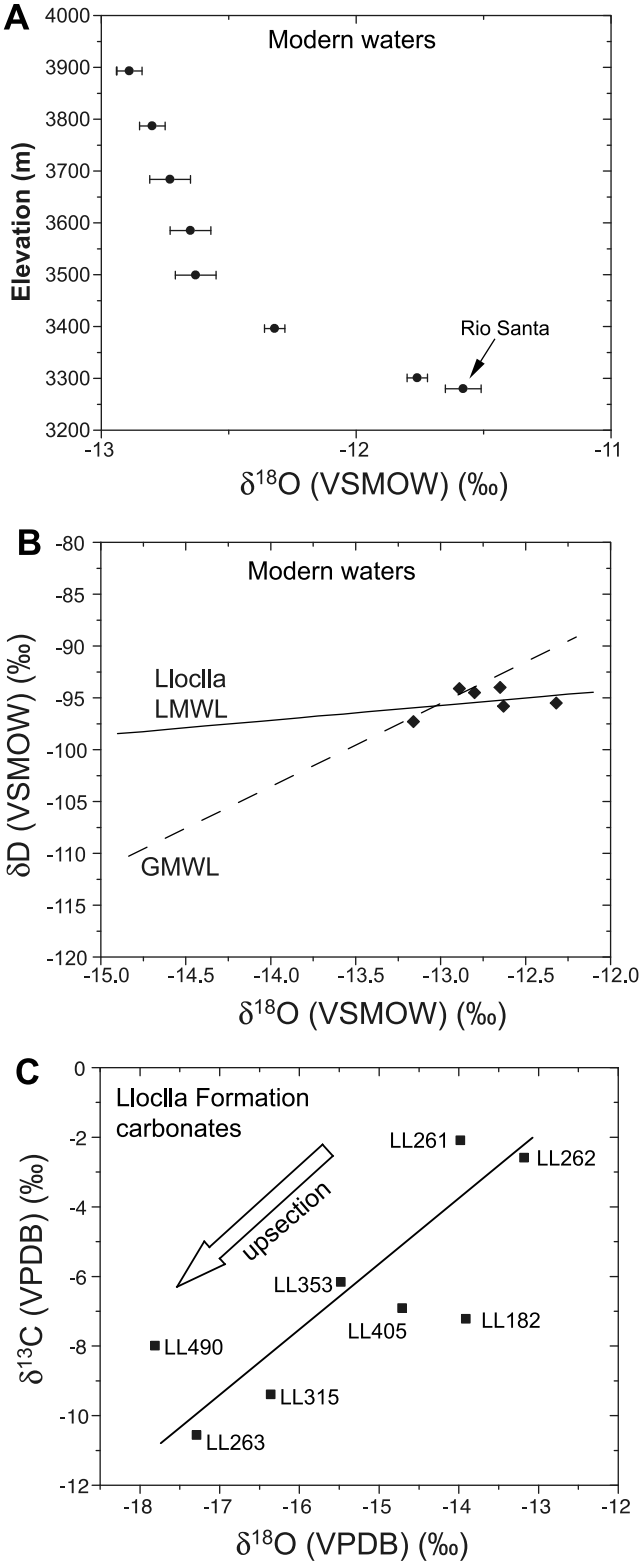

4.2. Oxygen and Hydrogen Isotopes of Modern Surface Waters

[36] Stable isotope paleoaltimetry was employed to evaluate surface uplift in the Cordillera Blanca. This method is based on analysis of stable oxygen isotopes (^{16}O and ^{18}O) in carbonates precipitated from surface waters. The $\delta^{18}O$ values of meteoric water ($\delta^{18}O_{mw}$) vary systematically with elevation, providing a means to reconstruct paleoelevation using $\delta^{18}O$ values of paleowaters [*Chamberlain and Poage*, 2000; *Garzione et al.*, 2000b; *Rowley et al.*, 2001; *Blisniuk et al.*, 2005]. As vapor masses ascend the flank of a mountain range, they expand and cool, causing rainout of heavier isotopes, thus producing lower $\delta^{18}O_{mw}$ values at progressively higher altitudes [*Gonfiantini et al.*, 2001; *Vuille et al.*, 2003]. Rayleigh distillation is considered to exert a primary control on the decrease in $\delta^{18}O_{mw}$ of meteoric water at higher altitudes in the Andes [*Gonfiantini et al.*, 2001; *Vimeux et al.*, 2005; *Rowley and Garzione*, 2007; *Sturm et al.*, 2007] with the caveat that changes in climate that alter the elevation-temperature gradient, seasonality of rainfall amount, or atmospheric circulation may affect the isotopic composition of source moisture or the isotopic lapse rate [e.g., *Vimeux et al.*, 2005; *Sturm et al.*, 2007; *Ehlers and Poulsen*, 2009; *Poulsen et al.*, 2010]. Stable isotope paleoelevation reconstructions are based on the observation that carbonates that precipitated from waters originating at higher altitudes yield more negative $\delta^{18}O$ values, as demonstrated by studies of both modern and ancient lacustrine and paleosol carbonates in contractional mountain belts [e.g., *Drummond et al.*, 1993; *Garzione et al.*, 2000a; *Rowley and Currie*, 2006; *Hoke et al.*, 2009].

[37] Paleoelevation can be estimated from oxygen isotope compositions of carbonates using a locally determined $\delta^{18}O$ versus altitude gradient and making reasonable assumptions about the past climate from available paleoclimate indicators [*Rowley and Garzione*, 2007]. However, additional considerations are required because other factors may also influence the $\delta^{18}O$ values of carbonate, including evaporative effects, diagenesis, and the temperature of calcite precipitation [*Garzione et al.*, 2004]. For accurate calibration of the local $\delta^{18}O$ versus altitude gradient, it is also necessary to collect modern water samples from a considerable range of elevations.

[38] In this study, modern water samples were collected in July 2005 from the <2 m wide by <30 cm deep trunk stream in Quebrada Llocla and analyzed for $\delta^{18}O$ values (Figure 10a). The $\delta^{18}O$ (VSMOW) values show a limited

Figure 10. Stable isotope results for modern stream waters of Quebrada Llocla and lacustrine carbonates of Llocla Formation. (a) Oxygen isotope results for modern stream waters showing more negative $\delta^{18}O$ values at higher elevation. (b) Comparative plot of oxygen and hydrogen isotope results for modern waters, showing $\delta^{18}O$ values versus δD (deuterium) values and resulting local meteoric water line (LMWL) relative to global meteoric water line (GMWL). (c) Comparative plot of oxygen and carbon isotope results for lacustrine carbonates, showing $\delta^{18}O$ values versus $\delta^{13}C$ values. Arrow denotes upsection trend toward more negative $\delta^{18}O$ values. Sample labels correspond to stratigraphic m level (Figure 5).

Table 6. Oxygen and Carbon Isotope Data[a]

Sample Name	Description	Sampling Elevation (m)	Stratigraphic Level (m)	$\delta^{18}O$ (VPDB) (‰)	$\delta^{13}C$ (VPDB) (‰)
LL182-C	micrite	3546	182	−13.9	−7.2
LL197-C	micrite	3561	197	−11.6	−6.7
LL199-C	micrite	3563	199	−11.0	−5.9
LL261-C	micrite	3625	261	−14.0	−2.1
LL262-C	micrite	3626	262	−13.2	−2.6
LL263-C	micrite	3627	263	−17.3	−10.6
LL315-C	micrite	3679	315	−16.4	−9.4
LL353-C	micrite	3717	353	−15.5	−6.2
LL405-C	micrite	3769	405	−14.7	−6.9
LL490-C	micrite	3854	490	−17.8	−8.0

[a]Quebrada Lloclla: 9°38.5′S, 77°29.3′W. Precision is better than ±0.05‰ for $\delta^{13}C$ and ±0.1‰ for $\delta^{18}O$ Vienna Pee Dee Belemnite (VPDB).

range between −11.5‰ and −13‰, with the most negative values observed at the highest elevations. The water samples were collected from the maximum elevation range of the Quebrada Lloclla stream, from the headwaters to the downstream confluence with the Rio Santa. Although this data set constrains modern surface water compositions along a single trunk river between 3250 and 3900 m elevation, the lack of samples from individual tributary streams at different elevations and the small ~650 m range in sample elevations limit robust estimates of the local $\delta^{18}O$ versus altitude gradient over a large range of elevations. Nevertheless, the $\delta^{18}O$ values are more negative with increasing elevation (Figure 10a), as predicted for modern stream waters.

[39] Hydrogen and oxygen isotopes of water are widely used as tracers of hydrological processes involving precipitation and interactions between groundwater and surface water [e.g., *Gibson et al.*, 2005]. The δD (deuterium) and $\delta^{18}O$ composition of global precipitation has been shown to vary systematically and define a uniform relationship in δD-$\delta^{18}O$ space called the global meteoric water line (GMWL) [*Gammons et al.*, 2006, and references therein]. It is recognized that the relationship between δD and $\delta^{18}O$ values of precipitation can vary regionally, necessitating the measurement of a local meteoric water line (LMWL) for comparison. The slope of the LMWL can depart from that of the GMWL due to evaporation under low humidity conditions and seasonal temperature variations. For modern waters of the Quebrada Lloclla, the slope of the LMWL is considerably lower than the GMWL (Figure 10b), suggesting evaporation under low relative humidity affected these waters. River waters were sampled in July 2005 during the dry season. At rainfall of <1cm/mo for June and July, as compared to 11–12 cm/mo in the summer rainy season[1], July represents the driest month of the year. Low rainfall rates associated with the season of sampling may account for the relatively positive $\delta^{18}O$ values and the low slope of the LMWL observed in stream waters.

4.3. Oxygen Isotopes of Lloclla Formation Carbonates

[40] Isotopic compositions of lacustrine carbonates commonly reveal a systematic correlation between carbon and oxygen isotopes [*Talbot*, 1990]. Such isotopic covariance can be attributed to closed basin conditions, recognizing that diagenetic alteration, mixing, and temperature variations may skew $\delta^{18}O$ and $\delta^{13}C$ values. In general, more positive values of $\delta^{18}O$ in lacustrine carbonates are likely associated with basin closure and an increase in the degree of evaporation [*Talbot*, 1990; *Drummond et al.*, 1995]. If the linear correlation coefficient (R^2) for covariance between $\delta^{13}C$ and $\delta^{18}O$ is >0.8, the carbonates were likely precipitated from a lake in a basin that experienced long periods of internal drainage. Moderately high covariance coefficients (R^2 ~ 0.6–0.7) suggest periods of extended residence times in lakes that existed in basins that were closed periodically [*Talbot*, 1990].

[41] Although the Callejon de Huaylas basin is dominated by conglomerate, eight levels of lacustrine carbonate were sampled within the Quebrada Lloclla section (Figure 5). Measured values of $\delta^{13}C$ and $\delta^{18}O$ are depicted on a single plot, with sample numbers corresponding to stratigraphic m level (Figure 10c and Table 6). The samples reveal $\delta^{18}O$ (VPDB) values ranging from −13.2‰ to −17.8‰. Assuming these carbonates were precipitated at temperatures similar to the modern summertime mean temperature of 12°C, when lake carbonates are most likely to precipitate [*Duston et al.*, 1986; *Effler et al.*, 1987], we calculate paleolake water compositions of −13.6‰ to −18.2‰(VSMOW) using the temperature dependent fractionation equation of *Kim and O'Neil* [1997]. The estimated lake water values are more negative than the $\delta^{18}O$ values of modern stream waters of -11.6‰ to −12.9‰. In lacustrine carbonate samples, the high degree of covariance (R^2 = 0.61) between $\delta^{13}C$ and $\delta^{18}O$ values is consistent with a lacustrine setting experiencing intermittent basin closure, possibly suggesting relatively high rates of evaporation at higher elevations. A moderate upsection decrease in $\delta^{18}O$ values from $\delta^{18}O$ (VPDB) = −11‰ to −14‰ in the lower part of the section to −14.7‰ to −17.8‰ in the upper part of the section (Table 6) is consistent with, but does not require, increased elevation in the source area with time. Likely alternatives include increasingly open lake conditions upsection or a climatic shift involving changes in the temperature of carbonate precipitation and/or rainfall amount. The isotopic composition of rainfall in tropical settings shows little to no correlation with air temperature but varies more as a function of rainfall amount and vapor mass history [*Rozanski et al.*, 1993; *Vimeux et al.*, 2005]. Assuming similar to modern surface water compositions would require that lake carbonates precipitated under cooler climate conditions. For example, if the most positive lake carbonates [$\delta^{18}O$(VPDB) = −13‰] reflect precipitation from the most positive surface waters [$\delta^{18}O$(VSMOW) = −11.5], then this would require a temperature of carbonate formation of 7°C. Although temperature proxy records and modeling of late Miocene climate in this region are lacking, the observation of warmer global climate in the late Miocene relative to today [e.g., *Zachos et al.*, 2001] suggests that 5°C cooler temperatures of carbonate precipitation is an unlikely cause of the discrepancy between modern waters and paleolake carbonates. A more likely scenario is that paleolake carbonates reflect lower $\delta^{18}O$ values of local meteoric water. An increase in the amount of precipitation or an increase in convective

Table 7. Oxygen Isotopic Data and Elevation Information for Sampled Modern Waters[a]

Sample Name	Stream	Sampling Elevation (m)	Sampling Location	δ^{18}O (VSMOW) (‰)	δD (VSMOW) (‰)
LL3280	Quebrada Lloclla	3280	S09°38.583′, W077°29.300′	−11.6	−92.9
LL3301	Quebrada Lloclla	3301	S09°38.485′, W077°29.083′	−11.8	−92.3
LL3396	Quebrada Lloclla	3396	S09°38.202′, W077°28.554′	−12.3	−94.7
LL3499	Quebrada Lloclla	3499	S09°37.322′, W077°28.298′	−12.6	−95.1
LL3585	Quebrada Lloclla	3585	S09°37.918′, W077°27.961′	−12.7	−93.8
LL3684	Quebrada Lloclla	3684	S09°38.029′, W077°27.685′	−12.7	−94.7
LL3787	Quebrada Lloclla	3787	S09°38.068′, W077°27.413′	−12.8	−95.0
LL3893	Quebrada Lloclla	3893	S09°38.239′, W077°27.200′	−12.9	−94.3
Drainage Basin	Area (km^2)	Sampling Season			
Rurec[b]	176.2	July 2005			

[a]Data for each location appear in order from lowest to highest sampling elevation. Elevations and locations were determined using a Garmin eTrex GPS unit. Precision is better than ±0.08‰ for δ^{18}O and ±1.4‰ for δD. VSMOW, Vienna standard mean ocean water.
[b]*Giovanni* [2007].

activity upstream of atmospheric flow provide more likely explanations of the lower δ^{18}O values of local rainfall in the late Miocene [*Vimeux et al.*, 2005; *Bony et al.*, 2008; *Risi et al.*, 2008]. Another potential source of the discrepancy between paleolake water and modern stream water is that modern stream waters appear to have experienced evaporation. As discussed in section 5.2, these waters were sampled during the dry season and are likely to reflect higher δ^{18}O values than precipitation during the summer rainy season. For a more accurate comparison of local meteoric water and paleolake water composition, modern streams should be sampled just following the summer rainy season (January–March). (Temperature and rainfall information for Chupaca, Peru, the nearest weather station of similar elevation to the Callejon de Huaylas basin (elevation = 3350 m) (www.weatherbase.com). Summertime mean temperature reflects the modern monthly mean temperature at Chupaca for the warmest 2 months (October and November).) To assess paleoelevation, we compare isotopic values of modern stream water (Figure 10a and Table 7) to those from uppermost Miocene carbonates of the Lloclla Formation (Figure 10c). Lloclla carbonates were deposited several Ma prior to the onset of regional glaciation at ~1.4 Ma [*Smith et al.*, 2005]. Given the extensive Quaternary glaciation in the Cordillera Blanca, the modern δ^{18}O values of stream waters sourced from snow-melt and glaciers [e.g., *Vimeux et al.*, 2009] should be more negative relative to ancient lacustrine waters from the same elevation. Furthermore, evaporative effects common to partially closed lake systems should result in enrichment in the δ^{18}O values of lake water. Both of these effects would tend to result in higher δ^{18}O values of paleolake waters relative to modern stream waters, leading to an underestimation of paleoelevation. The most negative paleolake water δ^{18}O values (~−18‰) from the uppermost Miocene Lloclla carbonates that likely exhibit the least evaporation are significantly more negative than modern stream waters (δ^{18}O values = −11.6‰ to −12.9‰ sampled during the dry season (Figures 10a and 10c), but similar in isotopic composition to ice cores in Peru that show δ^{18}O values between −16.5‰ and −20‰ [*Vimeux et al.*, 2009]. The similarity with modern ice core compositions suggests that surface waters reaching the lacustrine systems of the Callejon de Huaylas basin (Lloclla Formation) during the latest Miocene originated from elevations at least as high as the current elevation of the Cordillera Blanca.

5. Discussion

5.1. Basin Evolution

[42] Lithofacies, paleocurrents, and detrital provenance of the Lloclla Formation help delineate the depositional history of the Callejon de Huaylas basin in the hanging wall of the Cordillera Blanca detachment fault. ^{40}Ar/^{39}Ar results and upsection variations in stratal dip in the basin fill further constrain the timing and style of fault displacement.

[43] The Lloclla Formation contains an upward-coarsening, ~1300 m thick succession (Figure 5) that represents progradation of a stream-dominated alluvial fan into a lacustrine fan-delta system. Progradation is marked by an upsection transition from lacustrine mudstones, and localized carbonates, to thick cobble-boulder conglomerates with imbricated, rounded clasts. Paleocurrent data (Figures 5 and 8) for most of the formation indicate sediment dispersal to the NW in an axial to oblique direction relative to the NNW trending Cordillera Blanca. Sandstone and conglomerate provenance data (Figures 5 and 8) indicate a source region dominated by Tertiary volcanic rocks with increased input of sedimentary grains from the Cretaceous section and metasedimentary grains from the Jurassic interval. A considerable provenance change was recorded at the ~900 m level of the Lloclla Formation. Above this level, the appearance of granitic clasts and a shift toward more WSW directed flow suggest transverse sediment dispersal away from an uplifted footwall in which erosion had breached the Cordillera Blanca granitic batholith. This compositional trend indicates that the batholith was not a dominant source during most basin accumulation, in contrast to the modern drainages dominated by footwall granite clasts. Although significant variability characterizes the paleocurrents, conglomerate clast lithologies, and sandstone compositions (Figures 5, 7, and 8), the broad stratigraphic pattern defined by these data sets suggests that deeper levels of the footwall contributed greater proportions of sediment with time. We

interpret this unroofing pattern as the product of continued footwall exhumation during protracted west down motion on the Cordillera Blanca detachment fault (Figure 3).

[44] The timing of slip is constrained by the hanging-wall subsidence history. At the basin's type locality (Quebrada Lloclla; Figure 2), a tuff at the base of the Lloclla Formation yielded a $^{40}Ar/^{39}Ar$ biotite age of 5.4 ± 0.1 Ma (Figure 9d). This age is important because an unconformity at the base of the formation indicates the region underwent erosion after middle Miocene termination of deposition in the Calipuy Formation. Therefore, the basal Lloclla tuff represents a fundamental temporal shift toward deposition that marks the onset of fault-induced subsidence. We attribute initial hanging-wall subsidence of the Callejon de Huaylas basin at ~5.4 Ma to the onset of extension and detachment faulting in the Cordillera Blanca.

[45] Although local variations affect stratal dip within the Lloclla Formation, systematic measurements record dip variations that may be linked to the subsurface geometry of the Cordillera Blanca fault. Initial dips of 15°–25° are abruptly overlain by shallow dips (5°–10°) at 250–490 m, and then gradually steepen (~15°–30°) above 725 m (Figure 5). Dip shallowing at 250 m is consistent with growth strata deposited synchronously with hanging-wall tilting, most likely along a listric normal fault. Dip steepening above 490 m (Figure 5), although contrary to simple models of hanging-wall rollover, may indicate a ramp-flat fault geometry rather than a smooth curvilinear fault plane at depth [e.g., *Gibbs*, 1984].

5.2. Basin-Forming Mechanisms

[46] Although Quaternary glacial deposits cover large areas of the Callejon de Huaylas basin, the elongate supradetachment basin exhibits NW-SE differences suggestive of important along-strike variations in basin evolution and, by inference, the slip history along the ~200 km length of the Cordillera Blanca detachment fault. The southern Rio Santa valley contains the basin's type section in the form of the dominantly conglomeratic Lloclla Formation. This ~1300 m thick succession unconformably overlies volcanic rocks of the Eocene to middle Miocene Calipuy Formation. In contrast, the northern Rio Santa valley contains an up to 800 m thick succession of the upper Miocene (~7.5 Ma) Yungay ignimbrites, which unconformably overlaps the Jurassic-Cretaceous section. The Yungay ignimbrites are capped by glacial deposits, with no evidence of an intervening Lloclla Formation. Two possible models are presented to account for these along-strike discrepancies within the hanging wall of the Cordillera Blanca detachment fault.

[47] In the first model (Figure 11a), the normal fault acts as a single segment with one tip pinned and the other free to propagate. As the fault lengthens, the basin increases in length, width, and depth. Cumulative slip is greatest in locations closer the pinned fault tip and decreases in the direction of propagation. The result is a broadly synclinal basin geometry in longitudinal section that increases in amplitude and wavelength as the fault tip propagates [*Schlische and Anders*, 1996]. The active depocenter of the basin, defined by the location of maximum subsidence at any given time, migrates in the same direction as the propagating fault tip. The location of the active depocenter precedes the location of maximum cumulative fill thickness (Figure 11a). In addition, younger sediments will be deposited over a larger surface area than older sediments and will onlap onto older strata on the "trailing end" of the migrating depocenter. Ultimately, a longitudinal cross section will show stacking or "shingling" of progressively broader stratigraphic units such that the oldest units are exposed at the surface near the origination of slip but are buried by younger sediments farther along strike in the direction of depocenter migration and fault-tip propagation.

[48] In the second model (Figure 11b), multiple fault segments [e.g., *Dawers et al.*, 1993; *Densmore et al.*, 2004] that do not overlap in map view are each associated with their own isolated sedimentary basin. In the simple case of two faults, each fault propagates in both directions, with the oldest units restricted to the center of each subbasin (Figure 11b). As displacement accrues on the two fault segments, the fault tips propagate toward each other. Once the fault tips merge, new units are deposited basin-wide, thinning toward an intrabasin high. With further slip, the fault system now propagates as a single segment and strata begin to thicken toward the basin center [*Schlische and Anders*, 1996].

[49] Both models provide viable explanations for the along-strike (NW-SE) variations in the hanging wall of the Cordillera Blanca fault, notably the absence or presence of two major units, the Yungay ignimbrites and coarse-grained fill of the Lloclla Formation. We tentatively favor the first model involving a single fault segment that propagates to the SE because it can help account for the greater topographic relief and structural relief in the northern Rio Santa valley and Cordillera Blanca. However, a more definitive conclusion awaits more detailed information on spatial variations in fault displacement and basin thickness.

5.3. Modes of Synconvergent Extension

[50] The Cordillera Blanca is critical to understanding large-scale hinterland extension in convergent retroarc orogenic belts such as the Andes. Numerous hypotheses have been advanced to explain the driving mechanism(s) of extension in the Peruvian hinterland. Possible explanations include extensional collapse of thickened crust [*Dalmayrac and Molnar*, 1981; *Sebrier et al.*, 1988a, 1988b; *Mercier et al.*, 1992], normal reactivation of a preexisting fold-thrust structure [*Doser*, 1987; *Schwartz*, 1988; *Bellier et al.*, 1991], strike-slip partitioning along an obliquely convergent margin [*McNulty et al.*, 1998], kinematic linkages to flat-slab subduction of the oceanic Nazca plate [*McNulty and Farber*, 2002], or thermal weakening and failure due to pluton emplacement [*Petford and Atherton*, 1992]. Our sedimentologic, provenance, and $^{40}Ar/^{39}Ar$ results on the timing and mode of extensional basin development and our stable isotope data for basin fill offers new insights that bear on this problem.

[51] The structural and stratigraphic patterns of basin evolution in the Cordillera Blanca are compatible with classic models for supradetachment basins [e.g., *Friedmann and Burbank*, 1995]. The shallow fault dip (<40°), considerable dip-slip displacement (>10 km), relatively limited basin-fill thickness (<1.5 km), footwall-dominated sediment

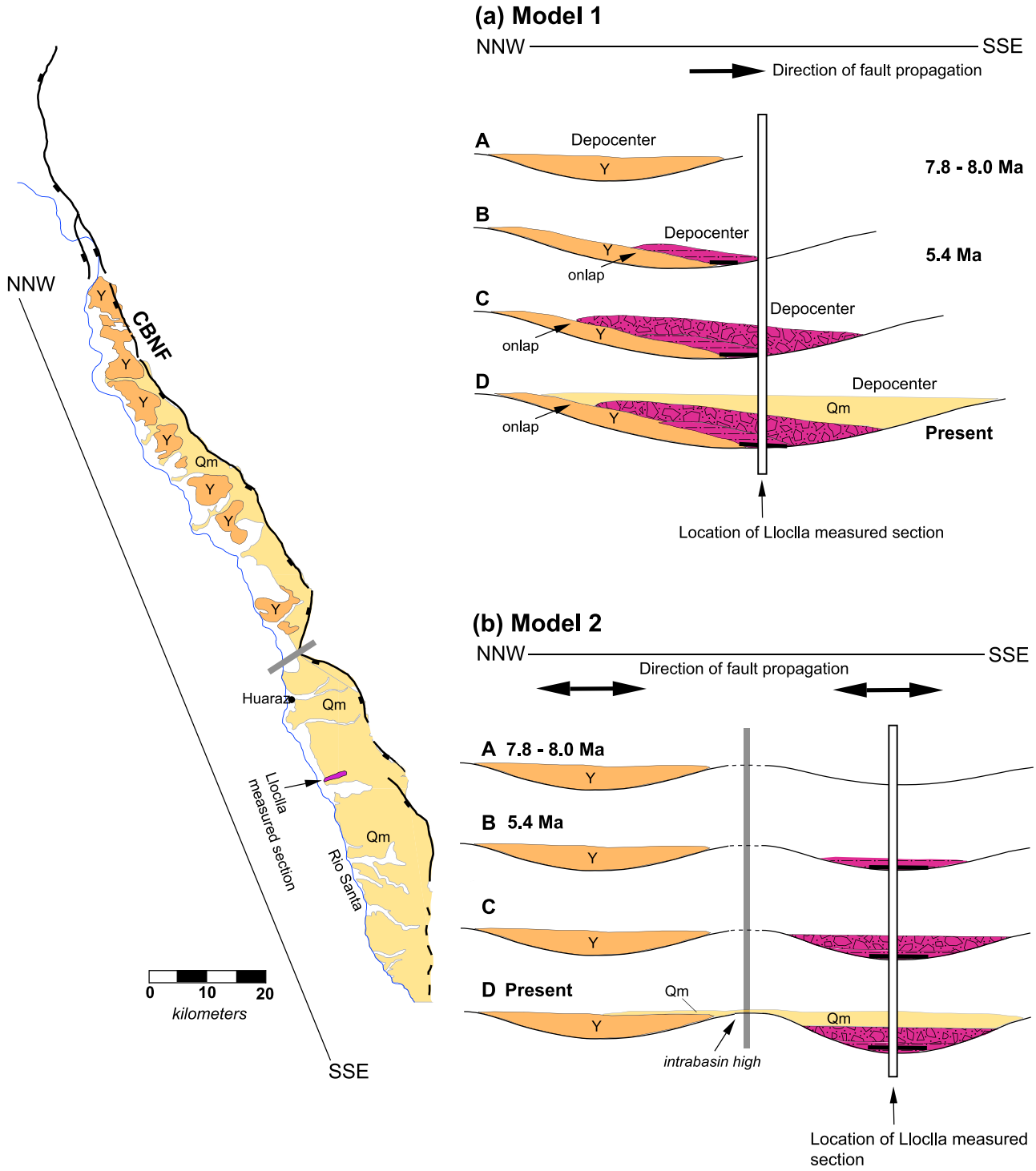

Figure 11. Schematic models of basin evolution linked to growth of the Cordillera Blanca normal fault. At left, a generalized map depicts fill of the Callejon de Huaylas basin, the bold black trace of the Cordillera Blanca normal fault (CBNF), the blue trace of the N-flowing Rio Santa, and the site of the Llocll a Formation measured section. Y = Yungay ignimbrite; Qm = Quaternary glacial deposits. (a) Model of a single, southward-propagating fault segment inducing southward migration of the basin depocenter. White bar denotes Llocll a measured section. (b) Model of two propagating fault segments inducing growth of two isolated extensional basins that coalesce into a single larger basin. Gray bar on map and cross section separates hypothesized fault segments.

supply, and existence of footwall mylonites are consistent with detachment-style faulting during large-magnitude extension. For the Cordillera Blanca, these criteria are inconsistent with deep transtensional (pull-apart) basins [e.g., *Mann et al.*, 1983], which are uncommon throughout the Andean hinterland [*Horton*, 2010]. In addition, the large displacement and existence of additional extensional structures in hinterland regions beyond the Cordillera Blanca [e.g., *Doser*, 1987; *Deverchere et al.*, 1989; *Bellier et al.*, 1991] suggest that extension is not governed by the local thermal effects of late Miocene emplacement of the Cordillera Blanca batholith. More generally, although low-angle normal faulting is commonly linked to broad regions of intercontinental extension such as the Aegean and Basin and Range provinces [e.g., *Coney*, 1987; *Buck*, 1991], we consider this detachment mode of extension to be equally applicable to deformation and basin growth in zones of synconvergent extension [e.g., *Robinson et al.*, 2004; *Kapp et al.*, 2008].

[52] Models linking extension in the Cordillera Blanca to plate-boundary processes rely on the timing of ridge collision and flat-slab subduction. For example, *McNulty and Farber* [2002] suggest that the Cordillera Blanca detachment fault may have been triggered by kinematic coupling with the shallowly subducted Nazca Ridge. Two recent reconstructions of the subduction history along the Peru trench [*Hampel*, 2002; *Rosenbaum et al.*, 2005] show that the buoyant Nazca Ridge migrated southward since initial collision with the Peruvian margin in the middle Miocene. Although there are minor differences, both reconstructions indicate that the subducted continuation of the Nazca Ridge passed beneath the Cordillera Blanca region by 15–10 Ma [*Hampel*, 2002; *Rosenbaum et al.*, 2005]. Our estimate of initial extension at ~5.4 Ma considerably postdates the timing of ridge passage and slab flattening beneath the Cordillera Blanca. Moreover, independent thermochronological evidence for rapid cooling in the Cordillera Blanca and adjacent Cordillera Huayhuash [*Garver et al.*, 2003, 2005; *Perry and Garver*, 2004; *Giovanni*, 2007], presumed to partially reflect fault-induced exhumation, consistently show fastest cooling over the past ~5 Ma.

[53] Most previous models suggest that surface uplift of the Cordillera Blanca was driven by activation of normal faulting and accompanying footwall rebound. However, considerations of gravitational body forces in a previously thickened crust [*Dalmayrac and Molnar*, 1981; *Suarez et al.*, 1983; *Molnar and Lyon-Caen*, 1988; *Sebrier et al.*, 1988b; *Mercier et al.*, 1992] suggest that extensional collapse yields little to no change in footwall elevation during the transition from preextensional to syn-extensional conditions. Oxygen isotope paleoaltimetry, when considered in light of possible climate change, diagenesis, and other influences, has the potential to test such predictions about paleoelevation. For the Cordillera Blanca, oxygen isotope values for lacustrine carbonates in uppermost Miocene basin fill are considerably more negative than modern stream waters (Figures 10a and 10c). Barring a significant warming of the regional climate, which would contradict recent studies [e.g., *Zachos et al.*, 2001; *Ehlers and Poulsen*, 2009; *Poulsen et al.*, 2010], these data suggest that the latest Miocene surface waters of the Callejon de Huaylas basin originated from elevations similar to, or possibly higher than, modern elevations of the Cordillera Blanca. Protracted high-altitude conditions in the Cordillera Blanca for the past ~5.4 Ma appear most consistent with models of orogenic collapse. In considering why Cenozoic large-magnitude extension did not affect other high regions of the Andes, we note that the Cordillera Blanca contains perhaps the greatest concentration of topography >5 km altitude in the orogenic belt. Nevertheless, a uniformly high region does not rule out the possibility of extensional reactivation of preexisting thrust structures in the Cordillera Blanca. Collectively, these findings suggest that a thickened crust with significant thrust-generated topography constituted a necessary condition for synconvergent hinterland extension in the Cordillera Blanca, similar to models of orogenic collapse for the North American Cordillera [*Coney and Harms*, 1984; *Coney*, 1987].

6. Conclusions

[54] 1. In the Andean hinterland of Peru, the Callejon de Huaylas supradetachment basin is located on the hanging wall of the active Cordillera Blanca normal fault, a WSW dipping, low-angle normal fault parallel to the regional strike of active fold-thrust structures farther east. The Cordillera Blanca and corresponding supradetachment basin represent a key example of active, detachment-style synconvergent extension in a modern retroarc hinterland.

[55] 2. Stratigraphy, sedimentology, paleocurrents, conglomerate clast compositions, and sandstone petrographic data help constrain the late Cenozoic evolution of the Callejon de Huaylas basin. The upper Miocene-Pliocene Lloclla Formation (~1300 m thick) records westward progradation of a stream-dominated alluvial fan and lacustrine fan-delta system away from the footwall. Paleocurrents and compositional provenance data record a shift in sediment dispersal patterns from NW directed to west directed at the ~900 m level. Above this level, the appearance of conglomerate clasts of the upper Miocene Cordillera Blanca batholith indicates initial exposure of the batholith during continued exhumation of the footwall of the Cordillera Blanca detachment fault.

[56] 3. The onset of hanging-wall subsidence is constrained by a new $^{40}Ar/^{39}Ar$ biotite age of 5.4 ± 0.1 Ma from the base of the Lloclla Formation. Initial subsidence of the supradetachment basin at ~5.4 Ma is attributed to the onset of extension along the Cordillera Blanca detachment fault. New $^{40}Ar/^{39}Ar$ ages from the Yungay ignimbrites in the northern basin reveal an earlier magmatic event between 10 and ~7.5 Ma, probably related to late Miocene emplacement of the Cordillera Blanca batholith.

[57] 4. Upsection variations in stratal dip within the Lloclla Formation define a hanging-wall growth stratal package indicative of active extensional faulting during basin filling. The Jurassic Chicama Formation serves as an approximate offset marker that yields an estimated minimum of 12–15 km of normal slip on the Cordillera Blanca detachment fault. Two alternative models invoking either a single propagating fault segment or multiple linking fault segments can help account for along-strike variations in

fault evolution that helped dictate the spatially variable accumulation histories within the supradetachment basin.

[58] 5. Oxygen isotope values from lacustrine carbonates in the Lloclla Formation indicate similar or more negative values than modern water, suggesting comparable (or possibly higher) elevations in the Cordillera Blanca during latest Miocene time. Protracted high-altitude conditions for the past ~5.4 Ma are consistent with models of orogenic collapse that account for the existence of synconvergent hinterland extension in the Cordillera Blanca.

[59] **Acknowledgments.** This work was initiated as part of a Ph.D. dissertation at the University of California, Los Angeles by M.K.G. under the supervision of B.K.H. Partial funding was provided by a National Science Foundation (NSF) Graduate Research Fellowship (M.K.G.), a Geological Society of America research grant (M.K.G.), and NSF grants EAR-0201937 (B.M. and B.K.H.) and EAR-0908518 (C.N.G. and B.K.H.). The manuscript was improved by constructive reviews of David Barbeau, Nadine McQuarrie, Todd Ehlers, and an anonymous associate editor. We appreciate beneficial discussions with Dan Farber, Stu Gilder, Bob Gillis, Mark Harrison, Paul Hoskin, Ray Ingersoll, Mick McRivette, Alex Robinson, and An Yin.

References

Axen, G. J., J. M. Bartley, and J. Selverstone (1995), Structural expression of a rolling hinge in the footwall of the Brenner Line normal fault, eastern Alps, *Tectonics*, *14*(6), 1380–1392, doi:10.1029/95TC02406.

Bellier, O., J. F. Dumont, M. Sebrier, and J. L. Mercier (1991), Geological constraints on the kinematics and fault-plane solution of the Quiches fault zone reactivated during the 10 November 1946 Ancash earthquake, northern Peru, *Bull. Seismol. Soc. Am.*, *81*, 468–490.

Blair, T. C., and J. G. McPherson (1994), Alluvial fans and their natural distinction from rivers based on morphology, hydraulic processes, sedimentary processes, and facies assemblages, *J. Sediment. Res.*, *64*, 450–489.

Blisniuk, P. M., L. A. Stern, C. P. Chamberlain, B. Idleman, and P. K. Zeitler (2005), Climatic and ecologic changes during Miocene surface uplift in the Southern Patagonian Andes, *Earth Planet. Sci. Lett.*, *230*, 125–142.

Bonnot, D. (1984), Neotectonique et tectonique active de la Cordillera Blanca et Callejon de Huaylas (Andes nord-peruviennes), Ph.D. thesis, 115 pp, Universite de Paris-Sud, Orsay.

Bonnot, D., M. Sebrier, and J. Mercier (1988), Evolution geodynamique plio-quaternaire du bassin intra-cordillerain du Callejon de Huaylas et de la Cordillere Blanche, Perou, *Geodynamique*, *3*(1–2), 57–83.

Bony, S., C. Risi, and F. Vimeux (2008), Influence of convective processes on the isotopic composition (delta O-18 and delta D) of precipitation and water vapor in the tropics: 1. Radiative-convective equilibrium and Tropical Ocean-Global Atmosphere-Coupled Ocean-Atmosphere Response Experiment (TOGA-COARE) simulations, *J. Geophys. Res.*, *113*, D19305, doi:10.1029/2008JD009942.

Buck, W. R. (1991), Modes of continental lithospheric extension, *J. Geophys. Res.*, *96*(B12), 20,161–20,178, doi:10.1029/91JB01485.

Burchfiel, B. C., Z. Chen, K. V. Hodges, Y. Liu, L. H. Royden, C. Deng, and J. Xu (1992), *The South Tibetan Detachment System, Himalayan Orogen: Extension Contemporaneous With and Parallel to Shortening in a Collisional Mountain Belt*, 41 pp, Geol. Soc. Am., Boulder, Colo.

Chamberlain, C. P., and M. A. Poage (2000), Reconstructing the paleotopography of mountain belts from the isotopic composition of authigenic minerals, *Geology*, *28*, 115–118.

Cobbing, E. J., and A. W. Sanchez (1996), Mapa geologico del cuadrangulo de Recuay, scale 1:100,000, digitized 1996, Instituto Geologico Minero y Metalurgico, Lima, Peru.

Cobbing, E. J., W. S. Pitcher, J. J. Wilson, J. W. Baldock, W. P. Taylor, W. McCourt, and N. J. Snelling (1981), *The Geology of the Western Cordillera of Northern Peru*, Institute of Geological Sciences, London.

Cobbing, J., A. Sanchez, W. Martinez, and H. Zarate (1996), *Geologia de los Cuadrangulos de Huaraz, Recuay, La Union, Chiquian y Yanahuanca*, 281 pp., Instituto Geologico Minero y Metalurgico, Lima, Peru.

Coney, P. J. (1987), The regional tectonic setting and possible causes of Cenozoic extension in the North American Cordillera, in *Continental Extensional Tectonics*, *Spec. Publ. Geol. Soc. London*, 28, edited by M. P. Coward, J. F. Dewey, and P. L. Hancock, pp. 177–186.

Coney, P. J., and T. A. Harms (1984), Cordilleran metamorphic core complexes: Cenozoic extensional relics of Mesozoic compression, *Geology*, *12*, 550–554.

Dalmayrac, B., and P. Molnar (1981), Parallel thrust and normal faulting in Peru and constraints on the state of stress, *Earth Planet. Sci. Lett.*, *55*, 473–481.

Dawers, N. H., M. H. Anders, and C. H. Scholz (1993), Growth of normal faults: Displacement-length scaling, *Geology*, *21*, 1107–1110.

DeMets, C., R. C. Gordon, D. F. Argus, and S. Stein (1994), Effect of recent revisions to the geomagnetic reversal time scale on estimates of current plate motions, *Geophys. Res. Lett.*, *21*(20), 2191–2194, doi:10.1029/94GL02118.

Densmore, A. L., N. H. Dawers, S. Gupta, R. Guidon, and T. Goldin (2004), Footwall topographic development during continental extension, *J. Geophys. Res.*, *109*, F03001, doi:10.1029/2003JF000115.

Deverchere, J., C. Dorbath, and L. Dorbath (1989), Extension related to a high topography: Results from a microearthquake survey in the Andes of Peru and tectonic implications, *Geophys. J. Int.*, *98*, 281–292.

Dickinson, W. R. (1985), Interpreting provenance relations from detrital modes of sandstones, in *Provenance of Arenites*, edited by G. G. Zuffa, pp. 333–361, Reidel, Dordrecht, Netherlands.

Doser, D. I. (1987), The Ancash, Peru, earthquake of 1946 November 10: Evidence for low-angle normal faulting in the high Andes of northern Peru, *Geophys. J. R. Astron. Soc.*, *91*, 57–71.

Drummond, C. N., B. H. Wilkinson, K. C. Lohmann, and G. R. Smith (1993), Effect of regional topography and hydrology on the lacustrine isotopic record of Miocene paleoclimate in the Rocky Mountains, *Palaeogeogr., Palaeoclimatol., Palaeoecol.*, *101*, 67–79.

Drummond, C. N., W. P. Patterson, and J. C. G. Walker (1995), Climatic forcing of carbon-oxygen isotopic covariance in temperate-region marl lakes, *Geology*, *23*(11), 1031–1034.

Duston, N. M., R. M. Owen, and B. H. Wilkinson (1986), Water chemistry and sedimentological observations in Littlefield Lake, Michigan—Implications for lacustrine marl deposition, *Environ. Geol. Water Sci.*, *8*, 229–236.

Effler, S. W., H. Greer, M. Perkins, S. D. Field, and E. Mills (1987), Calcium-carbonate precipitation and transparency in lakes—A case study, *J. Environ. Eng.*, *113*, 124–133.

Ehlers, T. A., and C. J. Poulsen (2009), Influence of Andean uplift on climate and paleoaltimetry estimates, *Earth Planet. Sci. Lett.*, *281*, 238–248.

Farber, D. L., G. S. Hancock, R. C. Finkel, and D. T. Rodbell (2005), The age and extent of tropical alpine glaciation in the Cordillera Blanca, Peru, *J. Quat. Sci.*, *20*(7–8), 759–776.

Friedmann, S. J., and D. W. Burbank (1995), Rift basins and supradetachment basins: Intracontinental extensional end-members, *Basin Res.*, *7*, 109–127.

Gammons, C. H., S. R. Poulson, D. A. Pellicori, D. A. Reed, A. J. Roesler, and E. M. Petrescu (2006), The hydrogen and oxygen isotopic composition of precipitation, evaporated mine water, and river water in Montana, USA, *J. Hydrol.*, *328*, 319–330.

Garver, J. I., C. R. Schiffman, and S. E. Perry (2003), Rapid tectonic exhumation of the Cordillera Blanca, Northern Peru, *Geol. Soc. Am. Abstr. Prog.*, *35*, 429.

Garver, J. I., P. W. Reiners, L. J. Walker, J. M. Ramage, and J. M. Perry (2005), Implications for timing of Andean uplift from thermal resetting of radiation-damaged zircon in the Cordillera Huayhuash, Northern Peru, *J. Geol.*, *113*, 117–138.

Garzione, C. N., D. L. Dettman, J. Quade, P. G. DeCelles, and R. F. Butler (2000a), High times on the Tibetan Plateau: Paleoelevation of the Thakkhola graben, Nepal, *Geology*, *28*, 339–342.

Garzione, C. N., J. Quade, P. G. DeCelles, and N. B. English (2000b), Predicting paleoelevation of Tibet and the Himalaya from d18O versus altitude gradients in meteoric water across the Nepal Himalaya, *Earth Planet. Sci. Lett.*, *183*, 215–229.

Garzione, C. N., P. G. DeCelles, D. G. Hodkinson, T. P. Ojha, and B. N. Upreti (2003), East-west extension and Miocene environmental change in the southern Tibetan plateau: Thakkhola graben, central Nepal, *Geol. Soc. Am. Bull.*, *115*, 3–20.

Garzione, C. N., D. L. Dettman, and B. K. Horton (2004), Carbonate oxygen isotope paleoaltimetry: Evaluating the effect of diagenesis on paleoelevation estimates for the Tibetan plateau, *Palaeogeogr. Palaeoclimatol. Palaeoecol.*, *212*, 119–140.

Gibbs, A. D. (1984), Structural evolution of extensional basin margins, *J. Geol. Soc.*, *141*, 609–620.

Gibson, J. J., T. W. D. Edwards, S. J. Birks, N. W. St. Amour, W. M. Buhay, P. McEachern, B. B. Wolfe, and D. L. Peters (2005), Progress in isotope tracer hydrology in Canada, *Hydrol. Processes*, *19*, 303–327.

Giovanni, M. K. (2007), Tectonic and thermal evolution of the Cordillera Blanca detachment system, Peruvian Andes: Implications for normal faulting in a contractional orogen, Ph.D. dissertation, 236 pp, Univ. of California, Los Angeles, Calif.

Giovanni, M. K., S. L. Beck, and L. Wagner (2002), The June 23, 2001 Peru earthquake and the southern Peru subduction zone, *Geophys. Res. Lett.*, *29*(21), 2018, doi:10.1029/2002GL015774.

Gonfiantini, R., M. A. Roche, J. C. Olivry, J. C. Fontes, and J. C. Zuppi (2001), The altitude effect on the isotopic composition of tropical rains, *Chem. Geol.*, *181*(1–4), 147–167.

Gutscher, M.-A., J.-L. Olivet, D. Aslanian, J.-P. Eissen, and R. Maury (1999), The "lost Inca Plateau": Cause of flat subduction beneath Peru?, *Earth Planet. Sci. Lett.*, *171*, 335–341.

Hampel, A. (2002), The migration history of the Nazca Ridge along the Peruvian active margin: A reevaluation, *Earth Planet. Sci. Lett.*, *203*, 665–679.

Hampton, B. A., and B. K. Horton (2007), Sheetflow fluvial processes in a rapidly subsiding basin, Altiplano plateau, Bolivia, *Sedimentology*, *54*, 1121–1147.

Hodges, K. V., and J. D. Walker (1992), Extension in the Cretaceous Sevier orogen, North American Cordillera, *Geol. Soc. Am. Bull.*, *104*, 560–569.

Hoke, G. D., C. M. Garzione, D. C. Araneo, C. Latorre, M. R. Strecker, and K. J. Williams (2009), The stable isotope altimeter: Do Quaternary pedogenic carbonates predict modern elevations?, *Geology*, *37*, 1015–1018.

Horton, B. K. (2010), Cenozoic evolution of hinterland basins in the Andes and Tibet, in *Recent Advances in Tectonics of Sedimentary Basins*, edited by C. Busby and A. Azor, Blackwell Sci., Cambridge.

Horton, B. K., and J. G. Schmitt (1996), Sedimentology of a lacustrine fan-delta system, Miocene Horse Camp Formation, Nevada, USA, *Sedimentology*, *43*, 133–155.

Ingersoll, R. V., T. F. Bullard, R. L. Ford, J. P. Grimm, J. D. Pickle, and S. W. Sres (1984), The effect of grain size on detrital modes: A test of the Gazzi-Dickinson point-counting, *J. Sediment. Petrol.*, *54*, 103–116.

Kapp, P., M. Taylor, D. Stockli, and L. Ding (2008), Development of active low-angle normal fault systems during orogenic collapse: Insight from Tibet, *Geology*, *36*, 7–10.

Kim, S. T., and J. R. O'Neil (1997), Equilibrium and nonequilibrium oxygen isotope effects in synthetic carbonates, *Geochim. Cosmochim. Acta*, *61*, 3461–3475.

Lavenu, A. (1986), Etude neotectonique de l'Altiplano et de la Cordillere Orientale des Andes Boliviennes, Ph. D. thesis, 433 pp, Universite de Paris-Sud, Orsay.

Leeder, M. R. (1999), *Sedimentology and Sedimentary Basins*, 592 pp., Blackwell Sci, Oxford.

Mann, P., M. R. Hempton, D. C. Bradley, and K. Burke (1983), Development of pull-apart basins, *J. Geol.*, *91*, 529–554.

McDougall, I., and T. M. Harrison (1999), *Geochronology and Thermochronology by the 40Ar/39Ar Method*, 2nd ed., 269 pp., Oxford Univ. Press, New York.

McNulty, B. A., and D. L. Farber (2002), Active detachment faulting above the Peruvian flat slab, *Geology*, *30*(6), 567–570.

McNulty, B. A., D. L. Farber, G. S. Wallace, R. Lopez, and O. Palacios (1998), Role of plate kinematics and plate-slip-vector partitioning in continental magmatic arcs: Evidence from the Cordillera Blanca, Peru, *Geology*, *26*(9), 827–830.

Mercier, J. L., M. Sebrier, A. Lavenu, J. Cabrera, O. Bellier, J-F. Dumont, and J. Machare (1992), Changes in the tectonic regime above a subduction zone of Andean type: The Andes of Peru and Bolivia during the Pliocene-Pleistocene, *J. Geophys. Res.*, *97*(B8), 11,945–11,982, doi:10.1029/90JB02473.

Miall, A. D. (1977), A review of the braided-river depositional environment, *Earth Sci. Rev.*, *13*, 1–62.

Miall, A. D. (1985), Architectural-element analysis—A new method of facies analysis applied to fluvial deposits, *Earth Sci. Rev.*, *22*(4), 261–308.

Miall, A. D. (1996), *The Geology of Fluvial Deposits*, 581 pp., Springer, Berlin.

Molnar, P., and H. Lyon-Caen (1988), Some simple physical aspects of the support, structure, and evolution of mountain belts, in *Processes of Continental Lithospheric Deformation*, 218, edited by S. P. Clark Jr., 179–207, Geol. Soc. Am. Spec. Pap., Boulder.

Nemec, W., and R. J. Steel (1988), What is a fan delta and how do we recognize it?, in *Fan Deltas: Sedimentary and Tectonic Setting*, edited by R. J. Steel and W. Nemec, pp. 4–13, Blackie, London.

Perry, S. E., and J. I. Garver (2004), Onset of tectonic exhumation of the Cordillera Blanca, northern Peru based on fission-track and U-Th/He dating of zircon, *Geol. Soc. Am. Abstr. Prog.*, *36*(2), 92.

Petford, N., and M. P. Atherton (1992), Granitoid emplacement and deformation along a major crustal lineament: The Cordillera Blanca, Peru, *Tectonophysics*, *205*, 171–185.

Poulsen, C. J., T. A. Ehlers, and N. Insel (2010), Onset of convective rainfall during gradual late Miocene rise of the central Andes, *Science*, *328*, 490–493.

Renne, P. R., A. L. Deino, R. C. Walter, B. D. Turrin, C. C. Swisher, T. A. Becker, G. H. Curtis, W. D. Sharp, and A. R. Jaouni (1994), Intercalibration of astronomical and radioisotopic time, *Geology*, *22*, 783–786.

Ridgway, K. D., and P. G. DeCelles (1993), Stream-dominated alluvial fan and lacustrine depositional systems in Cenozoic strike-slip basins, Denali fault system, Yukon Territory, Canada, *Sedimentology*, *40*, 645–666.

Risi, C., S. Bony, F. Vimeux, L. Delacroix, B. Ibrahim, E. Lebreton, I. Mamadou, and B. Sultan (2008), What controls the isotopic composition of the African monsoon precipitation? Insights from event-based precipitation collected during the 2006 AMMA field campaign, *Geophys. Res. Lett.*, *35*, L24808, doi:10.1029/2008GL035920.

Robinson, A. C., A. Yin, C. E. Manning, T. M. Harrison, S. H. Zhang, and X. F. Wang (2004), Tectonic evolution of the northeastern Pamir: Constraints from the northern portion of the Cenozoic Kongur Shan extensional system, western China, *Geol. Soc. Am. Bull.*, *116*(7–8), 953–973.

Rodbell, D. T. (1992), Late Pleistocene equilibrium-line-altitude reconstructions in the northern Peruvian Andes, *Boreas*, *21*, 43–52.

Rodbell, D. T. (1993), Subdivision of Late Pleistocene moraines in the Cordillera Blanca, Peru, based on rock-weathering features, soils, and radiocarbon dates, *Quat. Res.*, *39*, 133–143.

Rodbell, D. T., and G. O. Seltzer (2000), Rapid ice margin fluctuations during the Younger Dryas in the tropical Andes, *Quat. Res.*, *54*, 328–338.

Rosenbaum, G., D. Giles, M. Saxon, P. G. Betts, R. F. Weinberg, and C. Duboz (2005), Subduction of the Nazca Ridge and the Inca Plateau: Insights into the formation of ore deposits in Peru, *Earth Planet. Sci. Lett.*, *239*, 18–32.

Rowley, D. B., and B. S. Currie (2006), Palaeo-altimetry of the late Eocene to Miocene Lunpola basin, central Tibet, *Nature*, *439*, 677–681.

Rowley, D. B., and C. N. Garzione (2007), Stable isotope-based paleoaltimetry, *Annu. Rev. Earth Planet. Sci.*, *35*, 463–508.

Rowley, D. B., R. T. Pierrehumbert, and B. S. Currie (2001), A new approach to stable isotope-based paleoaltimetry: Implications for paleoaltimetry and paleohypsometry of the High Himalaya since the Late Miocene, *Earth Planet. Sci. Lett.*, *188*, 253–268.

Rozanski, K., L. Araguas-Araguas, and R. Gonfiantini (1993), Isotopic patterns in modern global precipitation, in *Continental indicators of climate, Proceedings of Chapman Conference*, *AGU Monogr.* 78, edited by P. Swart et al., pp. 1–36, Jackson Hole, WY.

Schlische, R. W., and M. H. Anders (1996), Stratigraphic effects and tectonic implications of the growth of normal faults and extensional basins, in *Reconstructing the History of Basin and Range Extension Using Sedimentology and Stratigraphy*, 303, edited by K. K. Beratan, Spec. Pap. Geol. Soc. Am., Boulder, Colo.

Schwartz, D. P. (1988), Paleoseismicity and neotectonics of the Cordillera Blanca fault zone, northern Peruvian Andes, *J. Geophys. Res.*, *93*(B5), 4712–4730, doi:10.1029/JB093iB05p04712.

Sebrier, M., J. L. Mercier, F. Megard, G. Laubacher, and E. Carey-Gailhardis (1985), Quaternary normal and reverse faulting and the state of stress in the central Andes of south Peru, *Tectonics*, *4*(7), 739–780, doi:10.1029/TC004i007p00739.

Sebrier, M., A. Lavenu, M. Fornari, and J.-P. Soulas (1988a), Tectonics and uplift in Central Andes (Peru, Bolivia, and Northern Chile) from Eocene to present, *Geodynamique*, *3*(1–2), 85–106.

Sebrier, M., J. L. Mercier, J. Marchare, D. Bonnot, J. Cabarez, and J. L. Blanc (1988b), The state of stress in an overriding plate situated above a flat slab: The Andes of central Peru, *Tectonics*, *7*(4), 895–928, doi:10.1029/TC007i004p00895.

Smith, J. A., R. C. Finkel, D. L. Farber, D. T. Rodbell, and G. O. Seltzer (2005), Moraine preservation and boulder erosion in the tropical Andes: Interpreting old surface exposure ages in glaciated valleys, *J. Quat. Sci.*, *20*(7–8), 735–758.

Sturm, K., G. Hoffman, and B. Langmann (2007), Climatology of stable water isotopes in South America: Comparing general to regional circulation models, *J. Clim.*, *20*, doi:10.1175/JCLI4194.1.

Suarez, G., P. Molnar, and B. C. Burchfiel (1983), Seismicity, fault plane solutions, depth of faulting, and active tectonics of the Andes of Peru, Equador, and southern Colombia, *J. Geophys. Res.*, *88*(B12), 10,403–10,428, doi:10.1029/JB088iB12p10403.

Talbot, M. R. (1990), A review of the palaeohydrological interpretation of carbon and oxygen isotopic ratios in primary lacustrine carbonates, *Chem. Geol.*, *80*, 261–279.

Uba, C. E., C. Heubeck, and C. Hulka (2005), Facies analysis and basin architecture of the Neogene Subandean synorogenic wedge, southern Bolivia, *Sediment. Geol.*, *180*, 91–123.

Vimeux, F., R. Gallaire, S. Bony, G. Hoffman, J. Chiang, and R. Fuertes (2005), What are the climate controls on isotopic composition (delta D) of precipitation in Zongo Valley (Bolivia)? Implications for the Illimani ice core interpretation, *Earth Planet. Sci. Lett.*, *240*, 205–220.

Vimeux, F., P. Ginot, M. Schwikowski, M. Vuille, G. Hoffmann, L. G. Thompson, and U. Schotterer (2009), Climate variability during the last 1000 years inferred from Andean ice cores: A review of methodology and recent results, *Palaeogeogr., Palaeoclimatol., Palaeoecol.*, *281*, 229–241.

Vuille, M., R. S. Bradley, M. Werner, M. Healy, and F. Keimig (2003), Modeling δ18O in precipitation over the tropical Americas: Part I. Interannual variability and climatic controls, *J. Geophys. Res.*, *108*(D6), 4174, doi:10.1029/2001JD002038.

Wells, M. L. (1997), Alternating contraction and extension in the hinterlands of orogenic belts: An example from the Raft River Mountains, Utah, *Geol. Soc. Am. Bull.*, *109*(1), 107–126.

Wilson, J. J. (1967a), Mapa geologico del cuadrangulo de Corongo, scale 1:100,000, Istituto Geologico Minero y Metalurgico, Lima, Peru.

Wilson, J. J. (1967b), Mapa geologico del cuadrangulo de Carhuaz, scale 1:100,000, Istituto Geologico Minero y Metalurgico, Lima, Peru.

Wilson, J. J. (1967c), Mapa geolgico del cuadrangulo de Huari, 1:100,000, Institudo Geologico Minero y Metalurgico, Lima, Peru.

Yonekura, N., T. Matsuda, M. Nogami, and S. Kaizuka (1979), An active fault along the western part of the Cordillera Blanca, Peru, *J. Geogr., Tokyo*, *88*, 1–19.

Zachos, J., M. Pagani, L. Sloan, E. Thomas, and K. Billups (2001), Trends, rhythms, and aberrations in global climate 65 Ma to present, *Science*, *292*, 686–693.

C. N. Garzione, Department of Earth and Environmental Sciences, University of Rochester, Rochester, NY 14620, USA.

M. K. Giovanni, Department of Geoscience, University of Calgary, Calgary, AB T2N 1N4, Canada. (mkgiovan@ucalgary.ca)

M. Grove, Department of Geological and Environmental Sciences, Stanford University, Stanford, CA 94305, USA.

B. K. Horton, Institute for Geophysics and Department of Geological Sciences, Jackson School of Geosciences, University of Texas at Austin, Austin, TX 78712, USA.

B. McNulty, Department of Earth Sciences, California State University Dominguez Hills, Carson, CA 90747, USA.